This paper must be cited as: Brites, C. D. S., Balabhadra, S., Carlos, L. D., Advanced Optical Materials 2019, 7, 1801239. https://doi.org/10.1002/adom.201801239.

Lanthanide-based thermometers: At the cutting-edge of luminescence thermometry

by Carlos D. S. Brites, Sangeetha Balabhadra and Luís D. Carlos*

Dr. Carlos Brites, Dr. Sangeetha Balabhadra and Prof. Luís Carlos
Department of Physics, CICECO-Aveiro Institute of Materials, University of Aveiro, Campus de Santiago, 3810–193 Aveiro, Portugal
E-mail: lcarlos@ua.pt

Keywords: luminescence thermometry, temperature, thermal imaging, lanthanide ions, nanothermometers

Abstract:

Present technological demands in micro and nanoelectronics, photonics, micro and nanofluidics, and biomedicine, among other areas, have reached a point such the use of conventional contact thermometers is not able to make measurements when spatial resolution decreases to the submicron scale. The development of novel non-contact thermal probes is, then, mandatory,

contributing for an expansionary epoch of luminescence thermometry. Luminescence thermometry based on trivalent lanthanide ions becomes very popular since 2010 due to the unique versatility, stability and narrow emission band profiles of the ions that cover the entire electromagnetic spectrum with relatively high emission quantum yields. Here we give a perspective overview on the field since the beginnings in the 1950's until the most recent cutting-edge examples. The current movement towards the use of the technique as a tool for thermal imaging, early tumor detection and as a tool for unveil properties of the thermometers themselves or of their local surroundings is also summarized.

https://doi.org/10.1002/adom.201801239

1. Introduction

Temperature, termed from Latin word "*temperātūra"* is an intensive physical quantity measuring the internal thermal energy state of a substance.[1] The statistical physics definition of temperature is the inverse of the derivative of the body's entropy *S,* with respect to its internal energy *U*, $T^{-1} = \partial S/\partial U$.[2, 3] Whereas body's entropy measures the amount of its atomic disorder, the temperature describes how strong the intensity of random submicroscopic motions of the body's particle constituents is. Understanding the temperature's central role and its precise and accurate measurement is vital across a broad spectrum of areas, such as automotive, aerospace and defense, metrology, climate, marine research, bio and nanomedicine, electronics, heating and cooling devices, production plants, and food's storage.[4-11] Presently, temperature sensors account for ~80% of the worldwide sensor market that is likely to grow to $6.86 billion by 2023, as recently estimated by Grand View Research[12] (Figure 1).

From the invention of thermoscope by Galileo until our days, many new methods and temperature sensors have been developed.[13] Generally, the temperature reading is achieved from an invasive probe material in direct physical contact with the body for which temperature is unknown. Although contact thermometers, such as thermocouples and thermistors, represent the major share of the present market, they require a thermal connection with the sample that disturbs the measurements in small systems being, in general, unsuitable for scales below 10 μm.[10, 14-21] Furthermore, these conventional thermometers require an electrical link in the sensor system that hamper their applications in conditions where electromagnetic noise is strong and sparks are hazardous.[4] Hence, such limitations of contact thermometers for small systems have been stimulating the development of new non-contact accurate thermometers with micrometric and nanometric spatial resolution, a challenging research topic under constant development in the last decade.[16-19, 21, 22] High-resolution non-contact thermometers operating at micro- and nanoscale have been categorized in many ways, as, for instance, depending on whether they make use of electrical or optical signals or are based on near- or far-field applications. However, each method, possesses several advantages as well as drawbacks and exhibit different spatial, temporal, and temperature resolution (see, for instance, Table 1 of ref. [10] for details).

Among noninvasive spectroscopic methods for determining temperature, the thermal dependence of phosphor luminescence – bandshape, peak energy and intensity, and excited states lifetimes and risetimes – is one of the most promising accurate techniques (often referred to as

thermographic phosphor thermometry). It operates remotely with high-detection relative thermal sensitivity (>1 %·K^{-1}) and spatial resolution (<10 μm) in short acquisition times (<1 ms), even in biological fluids, strong electromagnetic fields and fast-moving objects.[16-18] The most used approach to infer the absolute temperature from thermographic phosphor thermometry is to measure the luminescence intensities of two electronic transitions (occasionally involving Stark components of an excited electronic state) in thermal equilibrium (see Section 3). In fact, diverse phosphors capable of providing a contactless thermal reading through their light emission properties have been examined, e.g., polymers,[23-25] DNA or protein conjugated systems,[26] organic dyes,[27-29] quantum dots (QDs),[30, 31] Cr^{3+}-based materials,[32] and trivalent lanthanide (Ln^{3+}) ions (for a recent review see ref. [10]).

Organic dyes are the most available and used thermal probes; for a comprehensive review of the subject see, for instance, the works of Hoogenboom and collaborators.[33, 34] However, QDs and Ln^{3+}-based materials have been gaining relevance due to their higher photostability and relatively high emission quantum yields. For instance, QDs were employed in submicron thermometry due to its temperature-dependent luminescence features (intensity changes or emission peak shifts).[35, 36] Nanomedicine stands out as the most appealing area, since bioconjugation of QDs can make them target selective. However, QDs are often composed of highly cytotoxic elements (*e.g.* Cd) which makes difficult their future use in clinical trials.[37, 38] For a comprehensive review of the application of QDs in micro and nanothermometry see, for instance, the work of Jaque and collaborators.[39]

Ln^{3+}-based materials are versatile, stable and narrow band emitters covering the entire electromagnetic spectrum with, in general, high emission quantum yields (>50% in the visible).[40-46] A large number of Ln^{3+}-based molecular thermometers covering temperatures from the cryogenic (T<100 K) to the physiological (298–323 K) ranges have been reported, essentially in the last decade, involving chelate complexes,[14, 15, 47] metal organic frameworks (MOFs),[48-51] polymers,[52, 53] organic-inorganic hybrids,[47, 54] multifunctional heater-thermometer nanoplatforms,[55-57] and upconverting,[58-61] downconverting[62] and downshifting[63-66] nanoparticles (NPs). The implementation of these Ln^{3+}-based phosphors as ratiometric thermometers in diverse applications was extensively revised in the past decade,[7, 9, 10, 16-19, 21, 49, 51, 59, 67-82] including in two books.[83, 84]

The story of thermographic phosphor thermometry began in 1937 with Neubert[85, 86] during the development of the fluorescent lamp (for a review see the works of Allison and Gillies[4] and Khalid and Kontis[6]). The observed loss of luminescence intensity with increasing temperature suggested the use of phosphor luminescence as a nonintrusive technique for monitoring the temperature of hot bodies. In short, the temperature is rendered visible by optically projecting the bodies on an excited luminous screen and the image is produced by the extinction of the luminescence of the screen caused by the infrared radiation emitted from the hot body.[85, 86]

Twelve years later, Urbach *et al.* shown that the temperature-dependence of the luminescent efficiency of numerous phosphors could be used for the measurement of temperatures and temperature distributions, Figure 2.[87] The first applications, in aeronautics and medicine, date back to the 1950's and 1960's. In the former example, a phosphor was painted on the wing surfaces of a wind-tunnel model in order to probe the temperature, Figure 3,[88] while a couple of years later, and during the course of some studies on drug-induced tumor pain, it became clear that most breast cancers were characterized by an increase in temperature.[89] This heat elevation could be detected in the skin over the tumors and Lawson *et al.* in 1965 reported the employment of a thermally sensitive ZnCdS-based phosphor to record the human skin temperature, opening the avenue to apply thermography to clinical diagnosis, Figure 4.[89, 90]

After these pioneering works the interest on luminescent thermometers remains essentially flat until the 1990's, with less than 10 publications by year, Figure 5. In this period, mention must be done to some intriguing works on Ln^{3+}-based luminescent thermometers[91-93] and its applications in thermal imaging of surfaces[94, 95] and high-speed integrated circuits,[96] and to fiber tip thermometry systems. These last systems, commonly known as fluoroptic sensors, were initially proposed by Wickersheim and Alves[97] by applying a phosphor at the tip of an optical fiber, for a review see the work of Wickersheim and Sun.[98] In 1978, Luxtron (now LumaSense Technologies) industrialized the idea through the creation of its Fluoroptic® technology working through the $^5D_0$ decay time of $Gd_2O_2S:Eu^{3+}$.[99] Up to now, and as far as we know, this is the only commercial product based on luminescence thermometry. From 1995 to date the fluoroptic sensors have been extensively used in distinct thermal invasive procedures for tumor removal,[100] and for *in vivo* measurements of brain temperature.[101]

In 2002, a major breakthrough on the subject arised with the seminal paper of Wang *et al.* about using luminescent NPs for thermometry.[102] The temperature-dependent emission characteristics

of distinct semiconductor NPs were employed as a proof-of-concept and ratiometric luminescent thermometers were proposed for the first time based on $ZnS:Mn^{2+}$, Eu^{3+} NPs, in which the ratio of the emission intensities of the two dopants – the so-called fluorescence intensity ratio, FIR – provides robust temperature measurements. This concept was generalized a few years later to NPs doped only with Ln^{3+} ions ($BaTiO_3:Er^{3+}$ NPs).[103]

The topic has then exploded around 2010 (Figure 5), particularly due to the recognition of the enormous potential of luminescence thermometry in nanotechnology and nanomedicine. A few illustrative examples of important papers dated from that period involving Ln^{3+}-doped materials are:

- Phonon-induced heat generation and simultaneous noncontact temperature sensing Yb^{3+}/Er^{3+}-based upconverting nanoparticles (UCNPs)[104] and Nd^{3+}-based NPs;[105]
- Intracellular thermometers using Yb^{3+}/Er^{3+}-doped UCNPs;[61, 106]
- Eu^{3+}-doped organic-inorganic hybrid NPs for sensing and imaging of physiological temperatures;[47]
- Eu^{3+}/Tb^{3+}-doped organic-inorganic hybrid thermometers, including NPs[15] and MOFs;[107]
- *In vivo* imaging and temperature sensing using $Tm^{3+}/Er^{3+}/Ho^{3+}$-doped[108] and poly acrylic acid- coated Mo sensitized Yb^{3+}/Er^{3+}-doped NPs.[109]

Several reviews appeared on that explosion time (2010–2012), including examples on multiple optical chemical sensors,[110] inorganic phosphors that can withstand extreme temperatures,[69, 111, 112] luminescent and non-luminescent high-resolution micro and nanothermometers,[16-18, 70] UCNPs,[71] and temperature-stimuli polymers.[33, 113] After this period, the number of publications and corresponding citations has continued to grow exponentially, Figure 5a,b. Intriguing examples involving Ln^{3+}-doped materials are *in situ* measurements to visualize temperature gradients in photonic devices,[114, 115] microelectronic[116] and microfluidic[117] chips, catalytic processes,[118] dosimeters working in high-energy radiation fields,[119] and heated air jets and internal parts of combustion engines.[120] Currently, luminescence thermometry lives its inflationary epoch, with a total number of papers (citations) representing ~2.5% (2.0%) of the total number of papers (citations) published in the same period in the context of luminescence or luminescent systems, Figure 5c,d.

In the last couple of years, the focus of luminescence thermometry has gradually shifted from the synthesis and general characterization of new thermographic phosphors towards the use of the technique for thermal imaging, early tumor detection and as a tool for unveil properties of the thermometers themselves or of their local surroundings. In the former case, examples include acquisition of *in vivo* thermal images,[121-124] record of subcutaneous thermal videos[123] and *in vivo* ischemia detection in small animals.[124] Early tumor detection becomes possible by transient thermometry using NIR emitting Ag_2S nanocrystals.[125] Examples of the later approach are the analysis of heat transfer in heater-thermometer nanoplatforms,[126] the determination of the absorption coefficient and thermal diffusivity of tissues,[127] the measurement of the instantaneous ballistic velocity of Brownian nanocrystals suspended in both aqueous and organic solvents,[128] and the calculus of the thermal conductivity of porous silica and titania nanostructures[129] and the thermal resistance (in air) of NPs.[130] The present manuscript considers mainly these recent examples, being a follow up of the two books[83, 84] and the review papers published since 2015 on Ln^{3+}-based luminescent thermometers.[9, 10, 16-19, 21, 49, 51, 73, 78, 79, 81, 82]

https://doi.org/10.1002/adom.201801239

2. Classifying thermometers: *Primary and secondary thermometers*

There are many ways of sorting thermometers. Here, we list the most used classification regarding the way how the sensor is in physical contact with the probe and the intensity-to-temperature calibration relation.

Concerning the physical interaction between the thermal probe and the measurand, the thermometers can be classified as contact (evasive, *e.g.* thermocouples and thermistors) or non-contact (minimally evasive, *e.g.* infrared pyrometers). In between, semi-invasive thermometers are those in which there is contact between the sample and the probe, but the temperature is remotely interrogated. While the contact thermometers are well-suited for routine punctual measurements of non-moving systems, non-contact examples are appropriate for temperature measurements or mappings on moving objects or on objects in hazardous locations (*e.g.* thermal inspection of devices). The suitability of a given thermometer for an application is related to its sensing performance (*e.g.* operating range, thermal sensitivity, temperature uncertainty, acquisition rate, and spatio-temporal resolution), but also with the material's properties (*e.g.* physical state, simple and easy processable synthesis, facility to be implemented, and mechanical and thermal stability). Contact microscale and nanoscale thermal characterization techniques applied to active and passive devices and interconnects were reviewed by Christofferson *et al.*.[131]

Depending on the calibration relation, the temperature probes can be classified into primary and secondary thermometers. While the temperature is determined based on the knowledge of thermodynamic laws and quantities the thermometer is termed as primary. Contrary, if the temperature is calculated *via* comparison with a reference thermal probe, a calibration process is required and the thermometer is labeled as secondary.[132] Basically, whenever the knowledge of a measurable physical quantity is not enough to calculate the temperature from an equation of state (relating temperature with other measurable physical quantities), the thermometer must be referred to an external temperature reference and it is called secondary.

Up to know, five thermodynamic measurable quantities are used to determine temperature in primary thermometry: the pressure of a gas in a constant volume, the speed of sound in a monatomic gas, the dielectric constant of a gas, the black-body emission, and the power spectral density of Johnson-noise in an electrical resistor.[132, 133] Moreover, although primary thermometers are generally complex and mostly employed for metrology purposes, they are currently engaged

https://doi.org/10.1002/adom.201801239

in the redefinition of the international temperature scale (1990's International Temperature Scale or ITS-90) in terms of the Boltzmann constant (k_B).[134]

Examples of primary luminescent thermometers are, however, very scarce. Up to now, the reported examples are based on CdSe(ZnS) QDs,[135] Si NPs functionalized with 1-dodecene,[136] Y_2O_3:Eu^{3+} micro- and nanoparticles,[137] and SrF_2:Yb^{3+}/Er^{3+} UCNPs.[138] This last work, discussed in detail in section 3.1.1, is based on the Boltzmann law as the equation of state and is a major breakthrough on the subject. It demonstrates that any luminescent thermometer based on a ratio of intensities arising from two thermally-coupled emitting levels can be used to determine the temperature without a previous calibration procedure.

The most known secondary thermometers are electrical probes, such as platinum resistance thermometers, thermocouples, thermistors, capacitance thermometers and silicon diodes.[59] Although in general secondary thermometers are less complex than primary ones, recurrent calibrations are required, namely when the thermometers are used in a different medium than that in which they were calibrated. This is a tedious and time-consuming task that is not always possible to be implemented for luminescent thermometers, as, for instance, in living cells and in operating electronic devices. Indeed, many of the secondary thermometers reported in the literature assume valid a unique calibration relation, independent of the medium, a procedure potentially inaccurate (see section 3.1.1).

2.1. Performance of the thermometers

The quantitative comparison of the performance of any temperature probe is critical to evaluate its use and for the comparison between distinct techniques. Thermometers' performance can be evaluated based on its relative thermal sensitivity, temperature uncertainty, repeatability, reproducibility and spatio-temporal resolution. All the performance parameters for luminescent thermometers were recently reviewed[10] and, then, in what follows we only present a short summary highlighting the most important aspects.

2.1.1. Thermal sensitivity

The thermal sensitivity is the rate of change of the thermometric parameter (generally, designated by Δ), in response to the variation of temperature. The absolute thermal sensitivity (S_a) is expressed as:[139]

$$S_a = \frac{\partial \Delta}{\partial T} \quad (1)$$

depending only on the magnitude of the thermally induced variations in Δ. However, it is meaningless to quantitatively compare the thermal sensitivity among thermometers of different nature operating by different physical principles (*e.g.* optical, electrical, or mechanical thermometers) or, using the same physical principle, operate using different materials. To compare the performance of distinct thermometers, irrespectively of their nature or the material employed, the relative thermal sensitivity (S_r) should be adopted:

$$S_r = \frac{1}{\Delta}\left|\frac{\partial \Delta}{\partial T}\right|. \quad (2)$$

This parameter was introduced in 1998 by Collins *et al.,*[139] and has been extensively adopted as a figure of merit for the comparison of the thermometers' performance after the proposal of Brites *et al.* in 2012.[17] S_r is usually expressed in units of % change per degree of temperature change (%·K^{-1}), being the maximum value of S_r denoted by S_m.[10]

2.1.2. Temperature uncertainty

If S_r allows comparing the performance of different materials, the temperature uncertainty (or temperature resolution) δT describes the smallest temperature resolvable by the thermometer, depending not only on the material but also on the experimental setup used. The uncertainty in the temperature arise from several factors, such as the experimental detection setup, the acquisition conditions, and the signal-to-noise ratio. Usually, δT is estimated by the time-dependent output fluctuations of the thermometer calculating the evolution of the temporal fluctuations on the thermometric parameter. The temperature that corresponds to each Δ is obtained using a calibration curve (calculated from an equation of state in primary thermometers or empirically obtained in secondary examples), allowing the construction of a histogram of the temperature readouts during a certain time interval. The standard deviation of the resulting temperature histogram is the experimental δT of the thermometer. When this procedure is not possible to be implemented, an estimate for the temperature uncertainty is given by:[10]

$$\delta T = \frac{1}{S_r}\frac{\delta\Delta}{\Delta} \quad (3)$$

where $\delta\Delta/\Delta$ is the relative uncertainty in the determination of the thermometric parameter (determined by the acquisition setup, estimated from the errors in Δ). This value is controlled adjusting the signal-to-noise ratio in the acquisition of each emission spectrum that was used to calculate each Δ value, *e.g.* larger integration times and/or averaging consecutive measurements. Clearly, there is a compromise between dropping the temperature uncertainty and increasing the acquisition time: the longer is the acquisition time, the lower is the temperature uncertainty, being the minimum δT value that resulting from the standard deviation of the temperature histogram in the limit $t\rightarrow\infty$.

One interesting strategy to quantify the minimum temperature uncertainty of any thermometer was reported by Alicki *et al.* using the size and system-dependent properties and applying the spin-boson model.[140] For solid-state nanothermometers, the relative fluctuation in temperature is related to the number of atoms in the sample (N_A) and its Debye temperature (T_D):

$$\delta T = \left(\frac{4T}{3\sqrt{3}T_D}e^{\frac{3T_D}{8T}}\right)\frac{1}{\sqrt{N_A}}T. \quad (4)$$

For T_D in the range 100 to 2000 K the term in parenthesis changes between 0.9 and 1.3, meaning that the order of magnitude of the temperature uncertainty is essentially determined by:[140]

$$\delta T \sim \frac{T}{\sqrt{N_A}} \quad (5)$$

which means that the minimum achievable δT is fundamentally controlled by the size of the thermal probe.

In quantum metrology it is known that for non-entangled particles the precision $\delta\theta$ of a general quantity θ scales with the inverse of the number of particles (N_P):[141]

$$\delta\theta \sim \frac{1}{\sqrt{N_P}}, \quad (6)$$

a relation called shot-noise scaling (for entangled states, however, Heisenberg-scaling applies and $\delta\theta$ is inversely proportional to N_P). As N_P is proportional to N_A, Eq. 6 supports the result of the model derived by Alicki *et al.*[140] (Eq. 5).

There are very few examples reporting the thermal resolution of luminescent thermometers as a function of its size. One case is Alaulamie's work[142] that examined experimentally the correlation between particle size and the temperature uncertainty based on the temperature readouts of Er^{3+}-doped UCNPs clusters of different sizes (ranging from 1 to 9 μm). Briefly, the larger the cluster size the higher the signal-to-noise ratio, leading to smaller temperature uncertainties (low standard deviation value). The experimental data present an unequivocal increase of the temperature uncertainty as the cluster size decreases, in accord with Eq. 5 and Eq. 6. For the examples discussed above for which S_r increases as the size of the crystals decreases, Eq. 3 and Eq. 5 are only compatible if the decrease in $1/S_r$ is less than the increment of $\delta\Delta/\Delta$, resulting in an overall increase of δT with the decrease of N_A.

2.1.3. Resolution, reproducibility and repeatability

The spatial (δx) and temporal(δt) resolution of a measurement are defined as the minimum distance or time interval between measurements, respectively, presenting a temperature difference higher than δT.

The thermometer's reproducibility refers to the variation of the same measurement carried out under modified conditions (*e.g.* different equipment in use, different measurement methods, different observers, etc.).

The repeatability, R, describes the thermometer ability to provide repeatedly the same result, under the same circumstances and is computed by:

$$R = 1 - \frac{\max|\Delta_c - \Delta_i|}{\Delta_c} \quad (7)$$

where Δ_c and Δ_i represent, respectively, the thermometric parameter's mean value and the thermometric parameter measured at each temperature.

3. Sensing temperature with luminescence

Luminescence is affected by the temperature, among other external stimuli, and the induced changes can be monitored measuring distinct parameters of the emitting center, such as (i) the integrated emission intensity of a single transition or of a pair of transitions, (ii) the spectral shift, bandshape or bandwidth of a given transition, and (iii) lifetime measurements, using the decay profiles of emitting excited states (Figure 6). As the emission properties are characteristic of the emitting center itself, no fundamental limitations preclude the development of thermal probes with nanometric size. Luminescence thermometry exploits those emission temperature-induced changes either following the spectral changes of a given emission spectra (time-integrated scheme) or the temporal changes of a given transition (time-resolved scheme), as detailed in the next two sections.

3.1. Time-integrated schemes

Generally, the emission intensity of a given transition is sensitive to temperature changes due to the following mechanisms:

- Population redistribution over electronic levels accordingly to the Boltzmann statistics;
- Temperature-activated quenching mechanisms (*e.g.* cross-relaxation between electronic levels);
- Non-radiative deactivations (the electrons relax from excited states to the ground state generating heat, instead of light);
- Phonon-assisted Auger conversion processes.

Luminescent thermometers based on the emission intensity of a single transition depend critically on the illumination fluctuations, signal-to-noise detection, absorption and scatter cross-sections, and local changes of the phosphor concentration. Thus, end-user applications are not compatible with recursive calibration procedures and a ratio of intensities must be employed.[10, 18]

3.1.1. Intensity ratio (FIR) or bandshape

The bandshape-based nanothermometry exploits the relative change in the fluorescence intensity ratio of two independent energy-close transitions. Both emission lines can be generated from a single luminescent center (single-center thermometers) or they can result from two distinct emitting centers (dual-center thermometers).[16, 17] The use of single-center thermometers was described by Kusama *et al.*[91] in a seminal work; for a review of the technique see Collins *et al.*[143] and Wade *et al.*.[144]

In single-center ratiometric thermometers, Δ (or FIR) is defined using the emission intensities of the $|2\rangle\rightarrow|0\rangle$ ($I_{02}\equiv I_2$) and $|1\rangle\rightarrow|0\rangle$ ($I_{01}\equiv I_1$) transitions, where $|0\rangle$ denotes the ground level and $|1\rangle$ and $|2\rangle$ the two thermally-coupled excited levels:[144-146]

$$\Delta = \frac{I_2}{I_1} = \frac{A_{02} h\nu_{02}\, N_2}{A_{01} h\nu_{01}\, N_1} \quad (8)$$

where N_1 and N_2 are the populations of the $|1\rangle$ and $|2\rangle$ levels, h is the Planck constant, ν_{01} and ν_{02} are the frequencies of the $|1\rangle\rightarrow|0\rangle$ and $|2\rangle\rightarrow|0\rangle$ transitions, and A_{01} and A_{02} are the total spontaneous emission rates from levels $|1\rangle$ and $|2\rangle$ to level $|0\rangle$ (level $|2\rangle$ is more energetic than level $|1\rangle$). Note that Eq. 8 assumes that the intensities I_2 and I_1 are corrected by the instrument response. Furthermore, if the depopulation of the $|1\rangle$ and $|2\rangle$ energy levels involves other energy levels beyond $|0\rangle$, Eq. 8 must be corrected by the β_2/β_1 ratio, where β_i (i=1,2) are the branching ratios of the $|i\rangle$ level (*i.e.*, the percentage of the total emission from the thermalized level ($|1\rangle$ or $|2\rangle$) to the final $|0\rangle$ state). If the two levels are in thermal equilibrium (they are designated by "thermally-coupled levels", with separations of the order of the thermal energy), N_1 and N_2 are related by:

$$N_2 = \frac{g_2}{g_1} N_1 \exp\left(-\frac{\delta E}{k_B T}\right) \quad (9)$$

where g_1 and g_2 are the degeneracies of the two levels and δE is the energy difference between the barycenters of the $|1\rangle\rightarrow|0\rangle$ and $|2\rangle\rightarrow|0\rangle$ emission bands. Eq. 8 is, thus, written as:

$$\Delta = \frac{g_2 A_{02} h\nu_{02}}{g_1 A_{01} h\nu_{01}} \exp\left(-\frac{\delta E}{k_B T}\right) = B \exp\left(-\frac{\delta E}{k_B T}\right), \quad (10)$$

with $B = \frac{g_2 A_{02} \nu_{02}}{g_1 A_{01} \nu_{01}}$. The two levels cannot be too far apart, otherwise thermalization is no longer observed. For δE ranging from 200 to 2000 cm^{-1} the difference in the population of the emitting levels is such that they are considered "thermally-coupled" (*e.g.*, in a thermodynamically quasi equilibrium state). These empirical limits guarantee that the levels are spectrally separated and not too far away so that the exponential temperature decay rate (determined by δE) is small.[147]

Up to know, in most of the examples involving the temperature determination in single-center thermometers based on two thermally-coupled electronic levels δE and B are fitted parameters not determined independent of the temperature, and therefore, an external calibration of the thermal dependence of the thermometric parameter is needed. The standard calibration requires an independent measurement of the temperature (utilizing, for example, a thermocouple or an infrared camera) to permit the corresponding conversion between relative intensities and temperature. In this manner, a new calibration procedure is essential whenever the thermometer works in an alternate medium, as different factors, for example, the ionic strength, pH, pressure, ions local surroundings, or atmosphere composition, affect the thermometric parameter. As mentioned previously, recording multiple calibrations in various medium is a tedious task that is not always possible, and, generally, a single calibration relation is assumed to be valid, independent of the medium. This ad hoc assumption is a central bottleneck of secondary luminescent thermometers.

However, recently Balabhadra *et al.*[138] realized that δE and B can be measured independently of any experimental calibration procedure, demonstrating that single-center thermometers based on two thermally-coupled electronic levels are intrinsically luminescent primary thermometers. This was a significant step forward because it means that any thermometer based on Eq. 10 is, intrinsically, a primary thermometer, and, therefore, the equation can be used to predict the temperature calibration curve independently of the medium.[10, 138, 148] The energy gap δE is calculated using the formal definition of the barycenter of a *J*-*J'* transition (*J* is the total angular momentum) or, when there are experimental difficulties in assigning precisely the Stark-Stark transitions, by fitting the envelope of the I_1 and I_2 transitions,[63] see Figure 7a for the example of the $^2H_{11/2} \rightarrow {}^4I_{15/2}$ ($I_H \equiv I_2$) and $^4S_{3/2} \rightarrow {}^4I_{15/2}$ ($I_S \equiv I_1$) Er^{3+} transitions. The parameter B is empirically inferred from the plot of Δ versus laser excitation power, Figure 7b.[10, 138] In the limit of zero

excitation power, the temperature, T_0, corresponds to no laser-induced heating (the room-temperature[149, 150]) and the thermometric parameter Δ_0 is given by:

$$\Delta_0 = B \exp\left(-\frac{\delta E}{k_B T_0}\right). \quad (11)$$

The absolute temperature is directly determined by the Δ/Δ_0 ratio (calculated through the ratio between Eq. 10 and Eq. 11) as:

$$\frac{1}{T} = \frac{1}{T_0} - \frac{k_B}{\delta E} ln\left(\frac{\Delta}{\Delta_0}\right). \quad (12)$$

This approach was validated for the seminal example of the $^2H_{11/2} \rightarrow {}^4I_{15/2}$ ($I_H \equiv I_2$) and $^4S_{3/2} \rightarrow {}^4I_{15/2}$ ($I_S \equiv I_1$) Er^{3+} transitions ($^2H_{11/2}$ and $^4S_{3/2}$ are thermally-coupled energy levels[143, 145]) using SrF_2:Yb^{3+}/Er^{3+} UCNPs as an illustrative example (the Yb^{3+}/Er^{3+} ion pair is the most reported pair in Ln^{3+}-luminescent thermometry).[138] The temperature calculated through Eq. 12 was compared with the readout of conventional thermometers positioned in contact with the particles (for powders) or immersed in aqueous suspensions (Figure 7c). A remarkable agreement between the predicted and measured temperature values is observed, irrespectively of the NP's size and of the dispersion media, demonstrating that for this example no other variables apart temperature impact the thermometric parameter value. We should note that this approach is general and is extensible to any other thermometer based on two "thermally-coupled" levels, albeit up to now was solely applied to the $^2H_{11/2}$ and $^4S_{3/2}$ emitting levels.

The parameter B can be also calculated using the Judd−Ofelt theory.[151, 152] For that, let us consider the integrated coefficient of spontaneous emission of a transition between two manifolds J and J' as:[42, 153, 154]

$$A_{JJ'} = \frac{64\,\pi^4 e^2 \nu_i^3}{3\,h\,c^3}\left[\frac{n(n^2+2)^2}{9} S_{ed} + n^3 S_{md}\right] \quad (13)$$

where e is the electronic charge, c is the velocity of the light, and n is the refractive index of the medium. The electric (S_{ed}) and magnetic (S_{md}) dipole strengths are given (in units of e^2) by:

$$S_{ed} = \frac{1}{(2J+1)} \sum_{\lambda=2,4,6} \Omega_\lambda \left| \langle J' \| U^{(\lambda)} \| J^2 \rangle \right|^2 \tag{14}$$

$$S_{md} = \frac{h^2}{16\pi^2 mc^2} \left| \langle 0 \, || L + 2S || i \rangle \right|^2 \tag{15}$$

where the quantities Ω_λ (λ=2, 4, 6) are the so-called Judd–Ofelt intensity parameters[151, 152] and m is the electron mass. The $<||U^{(\lambda)}||>$ and $<||L+2S||>$ are reduced matrix elements (tabulated by Carnal *et al.*[155]) and the angular operators L and S are in units of h. The $\Omega_{2,4,6}$ parameters in Eq. 14 are phenomenologically obtained from the absorption[156] or, in the special case of the Eu^{3+} ion,[42] also from the emission spectra permitting the calculus of the coefficients of spontaneous emission and B parameter. For the $^2H_{11/2} \rightarrow {}^4I_{15/2}$ ($\nu_H \equiv \nu_2$) and $^4S_{3/2} \rightarrow {}^4I_{15/2}$ ($\nu_S \equiv \nu_1$) induced electric-dipole transitions, for instance, B is given by:[146, 157, 158]

$$B = \frac{\nu_2^4}{\nu_1^4} \frac{\beta_2}{\beta_1} \frac{\sum_{\lambda=2,4,6} \Omega_\lambda \left\langle {}^4I_{\frac{15}{2}} \left| \left| U^{(\lambda)} \right| \right| {}^2H_{\frac{11}{2}} \right\rangle^2}{\Omega_6 \left\langle {}^4I_{\frac{15}{2}} \left| \left| U^{(6)} \right| \right| {}^4S_{\frac{3}{2}} \right\rangle^2} \approx \frac{\nu_2^4}{\nu_1^4} \frac{\beta_2}{\beta_1} \frac{0.7158\,\Omega_2 + 0.4138\,\Omega_4 + 0.0927\,\Omega_6}{0.2225\,\Omega_6}. \tag{16}$$

Surprisingly, and as far as we know, this calculation has been scarcely reported. Three examples are Er^{3+}-based oxyfluoride glass and glass-ceramic[146] and $La_2S_3:Yb^{3+}/Er^{3+}$[158] and $SrF_2:Nd^{3+}$[159] crystalline powders.

3.1.2. Bandwidth

Generally, the emission lines of phosphors broaden as temperature increases. This is ascribed to the intrinsic vibrations of the lattice (homogeneous broadening, highly temperature dependent), or to the presence of different optical centers and defects (inhomogeneous broadening, slightly

temperature dependent). Henderson and Imbusch described the temperature dependence of the bandwidth (W) of emission and absorption bands as:[160]

$$W(T) = W_0 \sqrt{\coth\left(\frac{h\Omega}{2k_B T}\right)} \quad (17)$$

where W_0 is the full width at half maximum (FWHM) of the band at 0 K, and $h\Omega$ is the phonon energy (lattice vibration) that interacts with the electronic transitions.

There are few reports using intra 4f line's emission bandwidth to measure the temperature, despite all of them present the functional form predicted by Eq. 17. Strangely, none of these reports used Eq. 17 to extract the energy of the phonon responsible for the broadening. Peng *et al.*, for instance, used the $^5D_0 \rightarrow {}^7F_2$ transition in the $Y_2O_3:Eu^{3+}$ phosphor to determine the temperature in the 10–670 K range.[161] The transition bandwidth remains essentially unaltered for T<70 K, broadening linearly for higher temperatures at a rate of 0.078 $cm^{-1}\cdot K^{-1}$, corresponding to S_m=0.78 %$\cdot K^{-1}$ (at 70 K).[161] In another example, Wang *et al.* analyzed the bandwidth of several Tm^{3+} emission lines in $NaYbF_4:Tm^{3+}@SiO_2$ core@shell microparticles (Figure 8).[162] Among the transitions studied, the $^1D_2 \rightarrow {}^3F_4$ (350 nm) and $^3H_4 \rightarrow {}^3H_6$ (798 nm) ones broaden linearly with increasing temperature (100-700 K).[162] Using a $YAlO_3:Nd^{3+}$ nanoperovskite, Hernández-Rodríguez *et al.*[163] compared the thermometric performance of the material using the FIR method ($^2H_{9/2}$,$^4F_{5/2} \rightarrow {}^4I_{9/2}$/$^4F_{3/2} \rightarrow {}^4I_{9/2}$) and the FWHM of a Stark component of the $^4F_{3/2} \rightarrow {}^4I_{13/2}$ transition. The corresponding S_m values are 1.8%$\cdot K^{-1}$ and 3.3%$\cdot K^{-1}$, for the FIR method and the FWHM change, respectively (at 293 and 370 K, respectively). The corresponding temperature uncertainty values are 0.9 and 0.4 K. Although this example points out the benefit of using the spectral bandwidth approach for temperature determination, more studies are required to infer if this conclusion can be generalized for other systems.

Tm^{3+}-doped crystalline TiO_2 films[164] and the $[Eu(keto)_3(H_2O)]$[165] (keto=ketoprofen) coordination compound are interesting and atypical examples of Ln^{3+}-based luminescent thermometers reporting simultaneously temperature-induced bandwidth increase and wavelength shift. In the former example, the $^3F_{3,0\text{-}1} \rightarrow {}^3H_{6,0\text{-}1}$ Tm^{3+} transition (at 676 nm) exhibits a linear wavelength blue-shift $d\lambda/dT$ of −2.2 pm$\cdot K^{-1}$ (+0.048 $cm^{-1}\cdot K^{-1}$) with a 1.25 nm (55 cm^{-1})

bandwidth increase, over the ~85–750 K range. This linear behavior is in contrast with that exhibited by the convential $Al_2O_3:Cr^{3+}$ optically-based thermometers in which the peak-shift linear behavior only covers a limited region (~300–600 K), being the bandwidth and temperature precision highly affected at increasing temperatures.[164] For [Eu(keto)$_3$(H_2O)], whereas the FWHM of the $^5D_0 \rightarrow {}^7F_0$ Eu^{3+} transition shows minor variations (within the experimental resolution, ~3.0 cm^{-1}), its energy displays an approximately linear blue-shift as the temperature is raised from 25 to 300 K, maximum splitting of 16.6±3.0 cm^{-1}.[165] In both examples, the electron–phonon coupling seems to plays a relevant role in the mechanism beyond the temperature dependence of the Ln^{3+} transitions.

3.2. Time-resolved scheme: Lifetime

Unlike the luminescence intensity methods, the lifetime-based technique holds crucial advantage of virtually not being affected by the size, geometry and the concentration of the luminescent probe. Moreover, the value of lifetime shown to be independent on the effects of light scattering, reflection, and intensity fluctuation of excitation source. However, lifetime determination needs a pulsed excitation source with long illumination and acquisition time which in turn leads to time-consuming measurements limiting the use of this technique. Nevertheless, and although the thermal readout of large temperature gradients at time intervals shorter than or equal to the lifetime of the luminescence is impracticable using this technique, the recent technological advances made simpler and less expensive the employment of the technique.

3.3. Comparing the time-integrated and time-resolved schemes

Both the time-integrated and time-resolved temperature sensing methods show considerable potential and have been extensively studied for a wide range of materials.[10]. Even though the comparison between the performances of each method is intriguing, it has not been done systematically. One of the first examples was the pioneer work of Collins *et al.*[143] in Cr^{3+}-, Er^{3+}-, and Pr^{3+}-based crystals. The FTR response provides higher S_r values (*e.g.*, 5 times larger for the Pr^{3+}-based crystal). This is more evident for cryogenic temperatures as lifetime values are essentially temperature-independent in this range. The same conclusion was also inferred by Rai & Rai in Pr^{3+}-doped lithium tellurite glass,[166] Paviolo *et al.*[29] in fluorescent molecular thermometers based on rhodamine B (RhB) and by Gálico *et al.*[167] in the [Eu(bzac)$_3$(H_2O)$_2$]

complex (where $bzac^-$ stands for tris(1-phenyl-1,3-butanedione). Paviolo *et al.* realized that the temperature in the cytoplasm of an organic tissue accessed *via* RhB emission intensity is more accurate and reliable than that calculated using the RhB lifetime,[29] while Gálico *et al.* reported S_m=5.25%·K^{-1} (at 303 K) and S_m=1.35% K^{-1} (at 293 K)[167] through, respectively, the temperature dependence of the integrated intensity of the $^5D_0 \rightarrow {}^7F_2$ transition and of the $^5D_0$ lifetime. Recently, Gharouel *et al.*[168] performed a systematic comparison of the performance of distinct Pr^{3+}-based thermometers operating over 298–363 K using either the thermal dependence of the ratio of two 4f transitions or of the decay time of an excited state. Similar S_r values ranging from 0.25 to 0.60 %·K^{-1} were obtained and, again, although the lifetime approach requires more complex detection systems, the thermal sensitivity outcome is, at best, the same that the one obtained by the FIR method.[168] Therefore, in general, the wisest luminescence thermometry choice should produce a ratiometric intensity response to temperature changes.

4. Luminescent thermometers based on Ln^{3+} ions

4.1. Molecular complexes and organic-inorganic hybrids

Ln^{3+}-doped molecular systems (essentially with Eu^{3+} and Tb^{3+} ions) have been widely explored in luminescent thermometry, since the pioneering work of Sato *et al.* in 1989.[169] For a review on molecular Ln^{3+}-based thermometers see the work of Uchiyama *et al.*.[14] More recent noteworthy and illustrative examples are the works of Susuki *et al.*[170] and Hatanaka *et al.*.[171] The first example showed real-time thermogenesis in a single HeLa cell using the $Eu(tta)_3$ complex (tta^- stands for 3-thenoyltrifluoroacetonate) dissolved in dimethyl sulfoxide (DMSO). Temperature variations as small as 1 K in the physiological range were detected.[170] The second example uses $[Tb_{0.99}Eu_{0.01}(hfa)_3(linker)]_n$ polymers (where hfa^- stands for hexafluoro acetylacetonate and four phosphine oxides were used as linkers) – so-called chameleon emitters, because the emission color gradually changes with the temperature – to demonstrate how the thermal sensitivity is controlled by the linker, as well as by the hfa ligand.[171]

The chemical and optical instability of the isolated molecular systems,[172] however, preclude effective thermometry applications and composite materials formed by polymers or organic-inorganic hybrid hosts incorporating the lanthanoid complexes rapidly became an attractive alternative. An illustrative and pioneering example is the thermal imaging of a metal stripe covered with a thin film of poly(methyl methacrylate) (PMMA) doped with the $Eu(tta)_3$ complex.[94]

Despite the low temperature uncertainty (δT=0.08 K) and the quite interesting spatial resolution (δx=0.7 μm), the system is not ratiometric.

Using organic-inorganic hybrid materials as hosts, Brites *et al.*[15] proposed groundbreaking thermometers based on the Tb^{3+} ($^5D_4 \rightarrow {}^7F_5$) and Eu^{3+} ($^5D_0 \rightarrow {}^7F_2$) emissions, at 545 and 612 nm, respectively. The key point on this approach is the rational design of the host permitting the occurrence of thermally-driven $^5D_4 \rightarrow$host energy transfer, keeping the population of the $^5D_0$ emitting level unaffected. The $^5D_4 \rightarrow {}^7F_5/{}^5D_0 \rightarrow {}^7F_2$ relative intensity ratio guarantees, thus, the absolute measurement of temperature, with spatial resolution adjustable by the size of the nanoclusters to which the luminescent probes are anchored.[15] We should note that this mechanism is different than that usually observed in Tb^{3+}/Eu^{3+}-doped materials in which the temperature dependence of the $^5D_4 \rightarrow {}^7F_5/{}^5D_0 \rightarrow {}^7F_2$ intensity ratio is determined by Tb^{3+}-to-Eu^{3+} energy transfer mechanisms.[173] The use of Tb^{3+}-to-Eu^{3+} energy transfer as a tool to temperature sensing was firstly proposed by Sato *et al.* in 1989[169] and revisited by Liu *et al.* in 2005.[174] Nevertheless, and undoubtedly inspired by the works of Sato *et al.*[169] and Brites *et al.*,[15] the $^5D_4 \rightarrow {}^7F_5/{}^5D_0 \rightarrow {}^7F_2$ intensity ratio is by far the currently most used thermometric parameter allowing in the 298–333 K range typical values of S_m=7.1±0.2%·K^{-1}, δT=0.09±0.01 K, R>99.2%,[129] δx>0.5 μm, and δt>0.005 s.[116] For a review on luminescent thermometers based on organic–inorganic hybrids see Ref. [76].

Recent examples on Tb^{3+}/Eu^{3+}-doped systems not discussed in this review and deserving remark are the works of Piñol *et al.*,[126] Brites et *et al.*,[129] Rodriges *et al.*,[175] and Ramalho *et al.*.[176] The first two examples are discussed in more detail in section 5.2. Rodriges *et al.*[175] reported the thermometric functionalization of a Si surface with Tb^{3+} and Eu^{3+} complexes leading to S_m=1.45 %·K^{-1}, cycle-recycle reliability of 98.6 % and δT=0.3 K. The system is characterized by a dual-sensitive regime resulting from the hysteresis of its photoluminescence. The observed reversible bistability permits that the Si-functionalized surface can operate as an optically active two-module molecular demultiplexer logic circuit, opening the possibility of use this computing molecule in medical- and biotechnologies, such as blood diagnostics, “lab-on-a-molecule” systems, and molecular computational identification of small objects. On the other hand, Ramalho *et al.*[176] used a PMMA substrate coated with Tb^{3+}/Eu^{3+}-doped organic-inorganic hybrids to fabricate luminescent Quick Response (QR) codes.[176] QR codes are two-dimensional barcodes composed of special geometric patterns of black modules in a white square background that can encode

different types of information with high density and robustness. The strategy to multiplex distinct colored QR codes consisted in overlapping a base QR code with a luminescent one. Under daylight the PMMA-based luminescent code is transparent and the base code is readily accessed, whereas under UV illumination the PMMA-based QR code is luminescent enabling the color-multiplexing of the overlapped codes. The color multiplexing permits to increase the storage capacity per unit area of the luminescent QR codes by a factor of two, when compared to conventional QR codes. Moreover, the thermal dependence of the emission Commission Internationale de l'Elcairage (CIE) color coordinates enables the use of the QR code to sense temperature (reproducibility higher than 93%), opening new fields of applications for QR codes as smart labels for sensing.[176]

MOFs are a class of porous hybrid materials consisting of metal ions or clusters coordinated to organic ligands.[177] In particular, MOFs are excellent platforms for engineering luminescence properties as their building blocks, metal ions, linkers and guest ions or molecules, are all potential sources of light emission.[178-180] Because the luminescence of certain Ln^{3+}-bearing MOFs changes considerably with temperature, these materials have been explored in the last years as luminescent thermometers, especially based on the intensity ratio of two intra-4*f* transitions. The first reports on the subject by Cui *et al.*[178, 179] and Cadiau *et al.*[50] (first Ln^{3+}-bearing nanoMOF working as luminescent thermometer) used the intensity ratio of the Tb^{3+} ($^5D_4 \rightarrow {}^7F_5$) and Eu^{3+} ($^5D_0 \rightarrow {}^7F_2$) emissions, following up closely the ideas reported by us a couple of years before.[15] Nonetheless the MOF characteristic limited thermal stability precludes effective thermometry applications much above room-temperature, they are promising and even competitive with other thermometer materials in the cryogenic (<100 K) and biological (298–323 K) temperature ranges. In fact, we should note that among Ln^{3+}-based materials, Ln^{3+}-containing MOFs present the highest relative thermal sensitivity values reported so far, both in the cryogenic, S_m=31 %·K^{-1} (at 4 K),[181] and in the physiological, S_m=16 %·K^{-1} (at 300 K),[182] ranges. Cui *et al.*[49] and Rocha *et al.*[51] reviewed recently the main concepts and ideas assisting the design of MOF-based thermometers.

Recent examples on Tb^{3+}/Eu^{3+}-doped systems not discussed in these reviews and deserving remark are the works of Liu *et al.*[183] and Li *et al.*.[184] The first paper reported an *in situ* reduction and crystallization route for preparing Eu^{2+}/Eu^{3+}-doped MOFs. The materials exhibit intrinsic- and sensitized-emissions of Eu^{2+} and Eu^{3+} ions, besides a long-lived luminescence from ligand-to-metal charge transfer. A ratiometric luminescent thermometer was demonstrated based on the linear relation between temperature and the intensity ratio of Eu^{3+} (at 618 nm) and Eu^{2+} (at 427

nm) emissions between 9 and 293 K.[183] The second example described a MOF-based thermometer based on Eu^{3+}-to-ligand back energy transfer and operative over a wide temperature range including the physiological (12-320 K), upon excitation with visible light (450 nm).[184]

4.2. Upconversion (UC) and upconverting nanoparticles (UCNPs)

Upconversion (UC) emission is a nonlinear process developed by Bloembergen,[185] Auzel,[186] and Ovsyankin and Feofilov.[187] The distinct mechanisms of UC emission were extensively reviewed in the last years[188] and there are a great number of Ln^{3+}-based UCNPs that were proposed for luminescence nanothermometry. The UC emission can be distinguished as single-center and multi-center, depending on whether the UC signal is generated by a single type of Ln^{3+} ion or by a combination of different Ln^{3+} ions. Interestedly, and as far as we know, there is no examples reported in the literature of downconverting luminescent thermometers.

4.2.1. Single-center UC nanothermometers

The most common UC systems are based on Yb^{3+} as a sensitizer and Er^{3+}, Ho^{3+} or Tm^{3+} as activators. Yb^{3+} acts as an effective sensitizer owing a large absorption cross-section at 980 nm, a wavelength easily available due to its use in telecommunications technology. Furthermore, the Yb^{3+} excited state energy level matches well with the excited states of the Er^{3+}, Tm^{3+} and Ho^{3+} thus allowing an efficient resonant energy transfer.

As an activator, Er^{3+} is one of the widely used ion due to its strongly temperature-dependent intense green emission arising from the $^2H_{11/2}\rightarrow{}^4I_{15/2}$ (515-525 nm) and $^4S_{3/2}\rightarrow{}^4I_{15/2}$ (535-545 nm).[143, 145] Based on that emission, Rodrigues *et al.* measured one of the highest S_r values reported so far for upconversion thermal sensing using β-$NaGd_{0.94}Pr_{0.02}Er_{0.02}Yb_{0.02}F_4$@$3NaY_{0.8}Yb_{0.2}F_4$ core@shell NPs.[190] Under 980 nm irradiation, the visible Er^{3+} emission shows a relative thermal sensitivity in the 83−323 K range, reaching S_m=9.52·%K^{-1} (at 83 K). The intensity of those Er^{3+} transitions together with that of the Eu^{3+} $^5D_0\rightarrow{}^7F_2$ (603-643 nm) line were used by Nigoghossian *et al.*[189] to develop an intriguing example of a dual-mode nanothermometer. $NaGdF_4$:Yb^{3+}/Er^{3+} UCNPs were synthesized and coated with a silica shell to which a Eu^{3+} complex with tta was incorporated. Whereas the Er^{3+} UC emission was excited at 980 nm, the DS Eu^{3+} signal (not ratiometric) was excited at 352 nm through the tta ligands. Measurements were recorded near the physiological temperature range (293−323 K), revealing S_m=2.48·%K^{-1}/δT=0.47 K (980 nm) and

S_m=2.67·%K^{-1}/δT=0.06 K (352 nm), at 303 K. Moreover, the Eu(tta)$_3$-based complex present in the silica shell was tested as a UV sensor because of the Eu^{3+} luminescence dependence on UV-light exposure time. One of the limitations of the great majority of the nanothermometers fabricate up to now (including Er^{3+}-doped UCNPs) is a limited operating temperature range (typically not above 400 K), which prevents use in high-temperature applications, such as, for example, thermal barrier coatings and chemical reactors. Illustrative examples widening the temperature range of luminescent thermometers up to ca. 900 K are the works of Geitenbeek *et al.* in silica-coated $NaYF_4$:Yb^{3+}/Er^{3+} NPs,[191] Brites *et al.* in Sr_2GeO_4:Pr^{3+} crystalline powders[192] and Kolesnikov *et al.* in YVO_4:Nd^{3+}NPs.[193]

Tm^{3+} and Ho^{3+} are the other activator ions used for temperature sensing.[194-196] An illustrative example is the Y_2O_3:Yb^{3+}/Ho^{3+} submicron porous powders (978 nm excitation) reported by Lojpur *et al.*[195] that presents a maximum absolute sensitivity of 0.097 K^{-1}, at 85 K corresponding to S_m=1.61%·K^{-1}. Using the ratio between the intensity of the $^5F_4$,$^5S_2$→$^5I_8$ transition and that of distinct Stark components of the $^5F_4$,$^5S_2$→$^5I_7$ level in Ho^{3+}, yields to a maximum absolute sensitivity of Y_2O_3:Yb^{3+}/Ho^{3+} of 0.078 K^{-1}, that corresponds to S_m=0.55%·K^{-1}.

When the intensity ratio is taken from two transitions arising from thermally-coupled levels, the thermometric parameter is given by Eq. 10 and accordingly to the definition of S_r, Eq. 2, results:

$$S_r = \frac{1}{B\exp\left(-\frac{\delta E}{k_B T}\right)} \times \left|\frac{\partial B}{\partial T}\exp\left(-\frac{\delta E}{k_B T}\right) - B\frac{\delta E}{k_B T^2}\exp\left(-\frac{\delta E}{k_B T}\right)\right| = \left|\frac{1}{B}\frac{\partial B}{\partial T} - \frac{\delta E}{k_B T^2}\right|. \quad (18)$$

If B is temperature independent, S_r only depends on δE, decreasing monotonically with temperature increasing. On the contrary, if B is function of temperature, S_r also depends on the temperature dependence of the branching ratios of the two thermally-coupled levels, Eq. 16 (both the $\Omega_{2,4,6}$ parameters and the frequencies of the two transitions involved in the thermometric parameter are temperature independent). This dependence on the branching ratios of the two thermally-coupled levels might justify eventual changes on the S_r values with system's parameters, such as size, morphology, Ln^{3+} doping, or matrix's phonon energy.

The impact of nanoparticle's size on S_r values has been discussed in a few works.[103, 197, 198] The first reference dates back to 2004 reporting a size dependence on S_r values for $BaTiO_3$:Er^{3+}

nanocrystals in which the thermal parameter is the intensity ratio between the $^4S_{3/2} \rightarrow {}^4I_{15/2}$ and $^2H_{11/2} \rightarrow {}^4I_{15/2}$ Er^{3+} transitions.[103] As the size of the crystals decreases (from 60 to 26 nm) S_r increases, while the energy gap between the barycenters of the two transitions remains unchanged. Marciniak *et al.*[198, 199] also discussed a similar tendency in $NaYF_4:Yb^{3+}/Er^{3+}$ and $LiLaP_4O_{12}:Yb^{3+}/Er^{3+}$ nanophosphors. At 200 K, S_m raises from 1.1 %·K^{-1} to 2.1%·K^{-1}, as the size of fluoride nanocrystals decreases from 200 to 8 nm, and from 1.1 %·K^{-1} to 1.8%·K^{-1}, as the size of tetraphosphate nanocrystals decreases from 240 to 20 nm. An opposite trend, however, was reported by Dong *et al.*[197] on $NaYF_4:Yb^{3+}/Er^{3+}$ microspheres (size from 0.7 to 2 μm) showing that S_a decreases as size increases, S_m=1.4 %·K^{-1} (700 nm) and S_m=1.0 %·K^{-1} (1600 nm) (at 223 K), as calculated by us. Intriguingly, both trends were attributed to the larger specific surface area of the smaller crystals. As the size of the crystal decreases, a relatively large number of optically active ions are located at the surface and its contribution becomes increasingly important, being influenced by nonraditive relaxation channels related to electron–phonon interactions that are stronger with increasing temperature.[103, 197, 198] Moreover, the non-radiative rates of the two emitting levels might present a distinct temperature dependence and when the size of the nanoparticle decreases the material's phonons density changes inducing a dependence of those rates with the crystal size. However, Balabahadra *et al.*[138] and Brandão-Silva *et al.*[200] do not observe significant changes on S_r values with the decrease of the particle size in $SrF_2:Yb^{3+}/Er^{3+}$ (size from 10 to 41 nm) and $Y_2O_3:Er^{3+}$ (21 to 86 nm) NPs, respectively. Clearly, the influence of the nanoparticle's size on the thermal sensitivity of luminescent thermometers seems to be dependent of the host and of the electron-phonon interactions requiring a deep and systematic analysis.

In summary, single-centered UC thermometers are essentially being reported based on the analysis of the emission intensity of two thermally-coupled energy levels. Although these systems are intrinsically primary thermometers (see section 2), the tight restriction in the energy gap δE to ensure the strong coupling between the two levels, typically δE<2000 cm^{-1},[82] implies S_r values typically smaller than those characteristic of the downshifting examples (section 4.3). Larger energetic separation between the thermally-coupled levels decreases the thermalization of the upper energetic level, resulting in poorer luminescence intensity. To overcome this limitation, strategies for further S_r enhancement other than thermally-coupled levels for designing FIR-based thermometers should be considered, besides playing with the size of the NPs or with the phonon

energy of the hosts (as discussed above). A wisest approach consists in using two distinct (and thermally decoupled) emission lines of the same Ln^{3+} emitting center, or to use two emitting levels of distinct Ln^{3+} emitting centers, as discussed in the next section. The recent review by Cheng *et al.*[82] discusses strategies to improve S_r values by using thermometric parameters based on "fully-decoupled" or "moderately-coupled" emitting levels or emitting levels in which the energy transfer is mediated or thermally-assisted by a host or a ligand level.

4.2.2. Multi-center UC nanothermometers

Multicenter UC thermometry exploits the different thermal dependence of the intensity of two lines generated in distinct Ln^{3+} ions. The transitions can be fully thermally decoupled (*e.g.* both transitions decrease upon temperature raise) or can present an indirect thermal coupling (*e.g.* energy exchange mediated by the ion host or ligands). Both the possibilities have been reported extensively in the literature, being the energy transfer engineered *via* smart-chemical design of the thermal probe. The core@shell structure architecture allows a facile incorporation of dopants to guide an efficient energy transfer among different ions. Although multi-core@shell structures have been considerably reported for non-contact temperature measurements,[202, 203] there are only few works on multi-center UCNPs.[204-207]

An intriguing example was reported by Xu *et al.* using a Yb/Ho/Ce:$NaGdF_4$@Yb/Tm:$NaYF_4$ core@shell structure, presenting S_m=2.4 %·K^{-1} (at 298 K) in the absence of Ce^{3+}. The thermometric parameter is defined using the red (Ho^{3+}:$^5F_5 \rightarrow {}^5I_8$ and Tm^{3+}:$^1G_4 \rightarrow {}^3F_4$ transitions) and the green (Ho^{3+}: $^5S_2$,$^5F_4 \rightarrow {}^5I_8$ transition) bands. Introducing Ce^{3+} in the core the authors can tune S_m between 0.7 and 4.4 %·K^{-1} *via* the efficient cross relaxation processes between Ce^{3+} and Ho^{3+}(Figure 9).[206] Recently Savchuk *et al.*[130] reported $KLuWO_4$:Tm^{3+}/Ho^{3+} NPs as tunable multifunctional heater-thermometer nanoplatforms under 808 nm excitation. The intensity ratio is defined using the intensity of the Tm^{3+} $^3F_{2,3} \rightarrow {}^3H_6$ line (at 696 nm) and that of Ho^{3+} $^5S_2$,$^5F_4 \rightarrow {}^5I_7$ (at 755 nm) one, with S_m=2.8% K^{-1} and δT=0.2 K (at 300 K).

4.3.Downshifting (DS) and downshifting nanoparticles

Downshifting (DS) is a single photon process where upon excitation with a high-energy photon (typically in the UV region of the electromagnetic spectrum) a non-radiative relaxation takes place followed by radiative relaxation, thereby resulting in the emission of a lower-energy photon. As

an explanatory example we can mention the work of Ishiwada *et al.*[208] that reported $Tb^{3+}/Tm^{3+}:Y_2O_3$ NPs as visual thermo-sensors, working in the 323–1123 K range. The intensity ratio between the Tm^{3+} ($^1G_4 \rightarrow {}^3H_6$) and the Tb^{3+} ($^5D_4 \rightarrow {}^7F_5$) lines is strongly temperature-dependent, under 355 nm (UV) excitation with S_m=0.33%·K^{-1} (at 750 K). Lifetime based examples were also discussed, although in minor number, for the reasons addressed in section 3.3. The temperature dependence of the $^4S_{3/2}$ lifetime in the $NaY_2F_5O:Yb^{3+}/Er^{3+}$ NPs[58] presents S_m=2.75 %·K^{-1} (at 330 K), Figure 10. The authors tentatively attributed the shortening of the lifetime with the temperature increasing to non-radiative relaxation and multiphonon phenomena.

Several Ln^{3+} pairs were used for DS nanothermometry, such as Tb^{3+}/Eu^{3+},[15, 48, 50, 54] Nd^{3+}/Yb^{3+}[209], and Tm^{3+}/Ho^{3+}.[207] However, most of the examples discussed in recent years are based on Nd^{3+}, driven by potential bioimaging applications.[210] Nd^{3+} is of particular interest because of its ladder-like intra-4*f* levels which are amenable to NIR excitation (around 800 nm) and emission within the first (650–950 nm), second (1000–1400 nm), and third (1550–1870 nm) biological transparency windows, where the living tissues present low optical absorption.[211, 212] Nd^{3+} displays essentially five main transitions: $^4F_{5/2} \rightarrow {}^4I_{9/2}$ (800–850 nm), $^4F_{3/2} \rightarrow {}^4I_{9/2}$ (880–1000 nm), $^4F_{3/2} \rightarrow {}^4I_{11/2}$ (1000–1210 nm), $^4F_{3/2} \rightarrow {}^4I_{13/2}$ (1300–1480 nm) and $^4F_{3/2} \rightarrow {}^4I_{15/2}$ (1700–1850 nm), matching efficiently the three biological windows.[18, 81, 213] Most of the examples of thermometers based on DS are complex systems discussed in the following section.

4.4. Complex systems

In this section, we discuss illustrative examples of complex thermometric systems comprising multiple core@shell nanostructures,[214-217] polymer- and hybrid-based materials [30, 150, 218-221] and heater-thermometer nanoplatforms.[150, 222]

Multiple core@shell architectures are attracting much interest in recent years due to the possibility of combining distinct functions on a single nanostructure (see Ref. [216] for an updated review). An interesting approach is the use of these structures as double ratiometric nanothermometers. The first reported example used Yb^{3+}/Er^{3+} co-doped NPs covered with a Yb^{3+}/Nd^{3+} co-doped shell,[215] although more recently water dispersible nanoplatforms, with excitation and emission within the second and third biological optical transparency windows, were fabricated.[214] In the first example, temperature dependent Er^{3+} UC emission and Yb^{3+}/Nd^{3+} DS emission were observed with S_m=2.0 %·K^{-1} (at 200 K, Er^{3+}-based core thermometer) and

S_m=2.5 %·K^{-1} (at 365 K, Yb^{3+}/Nd^{3+}-based shell thermometer).[215] The second case comprises a core ($NaGdF_4$) co-doped with Er^{3+}/Ho^{3+}/Yb^{3+} followed by i) a first shell of Yb^{3+}; ii) a second shell co-doped with Yb^{3+}/Nd^{3+}, and iii) an additional passivation layer. The core@multishell structure was stabilized by a polyethylene glycol-grafted phospholipid and oleate. By using a heating-free 800 nm excitation, Ho^{3+}/Nd^{3+} (1180–1340 nm) and Nd^{3+}/Er^{3+}(1340–1550 nm) NIR emission band ratios were used for luminescence thermometry, both displaying similar relative thermal sensitivities (1.1% K^{-1}).[214]

Yang *et al.*[217] prepared by a multistep synthetic procedure a nanoplatform based on a Fe_3O_4 core coated by a middle SiO_2 shell and an $NaYF_4$:Nd^{3+} outer layer. The multi core@shell architecture showed excellent photostability, and impressive superparamagnetic properties (Figure 11). Under 806 nm continuous laser excitation the NPs exhibited three emission bands located within the NIR biological windows. The transparency of an *ex-vivo* tissue was tested presenting a clear larger penetration deep for λ<1200 nm, Figure 11.[217] Wang *et al.*[223] constructed a complex $NaLuF_4$:Gd^{3+}/Yb^{3+}/Er^{3+}@$NaLuF_4$:Yb^{3+}@$NaLuF_4$:Nd^{3+}/Yb^{3+}@$NaLuF_4$ core@shell system able of emitting both UC and DC luminescence under 808 nm excitation (Figure 12). The intensity ratio using the Yb^{3+} 980 nm ($^2F_{5/2}\rightarrow{}^2F_{7/2}$) and the Er^{3+} 1532 nm transitions ($^4I_{13/2}\rightarrow{}^4I_{15/2}$) was used for *in vivo* NIR imaging studies. An Er^{3+}-based UC nanothermometer using $NaLuF_4$:Yb^{3+}/Er^{3+}@$NaLuF_4$@Carbon core@shell@shell NPs with S_m=1.0 %·K^{-1} and δT=0.5 K (at 308 K) was reported by Zhu *et al.*.[57] The particles were internalized both *in vitro* and *in vivo* to obtain a temperature-feedback from real-time monitoring the microscopic temperature in photodynamic thermal therapy (Figure 13).

As mentioned previously, an important research line in Ln^{3+}-based luminescent thermometers explore the potential of polymers and organic-inorganic hybrids as host materials. The interesting example by Huang *et al.*[218] reported a hybrid nanocarrier consisting of Yb^{3+}/Er^{3+} co-doped $NaGdF_4$ NPs encapsulated in the aqueous core of liposomes. The 980 nm excitation is used simultaneously to induce the Er^{3+} green UC emission and for drug delivery, by co-loading the doxorubicin (DOX) model anticancer drug with the UCNPs in the liposome nanocarrier. Additionally, a quenching on the green emission was assigned to the energy transfer between the donor UCNPs and the acceptor DOX, allowing the spectral monitoring of the DOX loading and release from the liposome nanocarriers.[218] Although the authors do not report temperature determination the emission spectra of the nanoplatform can be also used with that purpose.

The combination of Ln^{3+}-based phosphors with other emitting centers was also exploited. Cerón *et al.*[53] developed a complex system combining Nd^{3+}-doped $NaGdF_4$ NPs and semiconductor PbS/CdS/ZnS QDs in a hybrid nanostructure formed by poly(lactic-co-glycolic acid). The thermometric parameter is based on the strongly temperature-dependent emission at 1220 nm (arising from the QDs) and a temperature-independent reference peak at 1060 nm (the Nd^{3+} $^4F_{3/2}\rightarrow{}^4I_{11/2}$ line). The coexistence of these two emissions allows to obtain S_m=2.5 %·K^{-1} (at 303 K).

Heater-thermometer nanoplatforms are other interesting systems because they combine the heat release and temperature monitoring in a single nanostructure. One of the most exploited strategies consists in use plasmonic nanostructures and luminescent thermometers to achieve a fully non-contact control of the system. One of the first examples was reported by Debasu *et al.*,[150] that developed a single nanoplatform integrating laser-induced heat generation by gold NPs and temperature sensing up to 2000 K *via* Gd_2O_3:Yb^{3+}/Er^{3+} nanorods. The temperature determination is done based on the green Er^{3+} upconversion emission and Boltzmann's law, for temperatures until 1200 K, and using the blackbody emission and the Planck's law of blackbody radiation for temperatures until 2000 K.

Other illustrative example combines Au nanorods and $NaGdF_4$:Yb^{3+}/Er^{3+} UCNPs.[222] The longitudinal surface plasmon resonance of the nanorods is tuned to 980 nm, in resonance with the Yb^{3+} absorption wavelength, so luminescence thermometry and heating can be simultaneously excited. As an added benefit the authors observe a luminescence enhancement until 9-folds due to the proximity of the Er^{3+} ions with the plasmonic structures. The temperature is controlled by the 980 excitation power and measured *in situ* by the Er^{3+} thermally sensitive luminescence.[222] In a step forward, the same group reported a nanocomposite consisting of $NaGdF_4$:Yb^{3+}/Er^{3+} nanoparticle, mesoporous SiO_2, Au nanorods and a photosensitizer. Under 980 nm irradiation, plasmonic and UC NPs are simultaneously excited leading to a plasmonic enhancement of the UC luminescence and a simultaneous temperature increasing. Upon laser irradiation, and after loading a Zn phthalocyanine photosensitizer into the mesoporous SiO_2, the UC visible light subsequently activates the photosensitizer to release reactive oxygen species.[224]

5. Current trends in lanthanide-based luminescent thermometers

As highlighted in the introduction, in the last couple of years the focus of luminescence thermometry has gradually shifted from the synthesis and general characterization of new thermographic phosphors towards the use of the technique as a tool in bioimaging, early tumor detection, and for unveil properties of the thermometers themselves or of their local surroundings. The present section covers meaningful examples demonstrating this shift. Moreover, the section also summarizes recent developments to boost the thermal sensitivity of luminescent thermometers.[225]

5.1. Luminescence thermometry using Ln^{3+} ions as a biomedical tool

Eu^{3+}-based thermometers were used to visualize the temperature-distribution within living organisms at microscopic scales. A polymer incorporating Eu-tris(dinaphthoylmethane)-bis-trioctylphosphine oxide as a temperature sensitive probe and rhodamine 800 (Rh800) to provide a reference emission band enabled the temperature monitoring and mapping with S_m=3.6 %·K^{-1} and 1.4<δT<1.0 K. The polymer embedding the thermal probes successfully detected *in vivo* temperature shifts at localized sites in the muscle of a living beetle, either due to an external heat source (980 nm laser heating) or due to the animal's voluntary muscle-activation (pre-flight preparation, Figure 14a-c). The Eu^{3+}/Rh800 intensity ratio was recorded in 5 distinct positions of the muscle (Figure 14d,e) presenting a dynamics similar to that monitored by an IR thermal camera.[122] Moreover, the same research group developed free-standing nanosheets embedding the same emitting centers with superior flexibility and transparency, compared with the previous report, enabling the attachment onto the uneven surfaced living tissues without any glue (Figure 15a,b) and the densification of muscle fibers covered by the thermometric film. The film was used to measure temperature shifts in a beetle's dorsal longitudinal muscle (Figure 15c,d) during the voluntary heat production, with S_m=3.75 %·K^{-1} at 302 K and δT up to 0.75 K. Endogenous heat production transfer between muscle fibers were studied using the thermal mapping recorded using the Eu^{3+}-Rh800 stacked nanosheets with a spatial resolution at least at the single muscle fiber level (impossible to achieved through IR thermal cameras), leading to further understand physiological activities in three stimulations: before, during and after the beetle's pre-flight preparation (Figure 15e).[121]

The absorption coefficient and thermal diffusivity of tissues was calculated by Ximendes *et al.*[127] using Yb^{3+}/Nd^{3+}-based thermal probes. The authors follow the time-dependent temperature relaxation process to calculate the thermal diffusivity of living tissues by luminescence thermometry (0.13 ± 0.04 $mm^2 \cdot s^{-1}$) in good agreement with that reported for breast tissue at 810 nm (0.142 $mm^2 \cdot s^{-1}$).[127]

Zhu *et al.* demonstrated a programmed combination of chemotherapy (CT) and photothermal therapy (PTT) combining in a single system, $NaLuF_4:Yb^{3+}/Er@NaLuF_4@Yolk\text{-}Shell\text{-}SiO_2$-PdPc@DPPC-DOX, UCNPs, a photothermal agent (octabutoxyphthalocyanine palladium (II), abbreviated as PdPc) and a thermal responsive drug release unit (1,2-dipalmitoyl-sn-glycero-3-phosphocholine, abbreviated as DPPC), as the vehicle of the DOX chemodrug, (Figure 16).[226] By controlling the nanostructure' temperature (using a 730 nm laser), the CT-PTT sequence can be designed to achieve programmed combination cancer therapy. When the dosages of DOX and heat are kept at low level (2.5 μM and 0.150 W cm^{-2}, respectively), programmed combination therapy can achieve 39 folds improvement in therapeutic effect *in vitro* in comparison with conventional combination therapy that simultaneously initiates CT and PTT.[226]

IR-emitting core@shell Er-Yb@Yb-Tm LaF_3 UCNPs were reported for subcutaneous thermal probing operating in the second and third transparency biological windows of tissues with thermal sensitivity of $5\% \cdot K^{-1}$. The acquisition of time-resolved 2D thermal images in a small animal model was reported taking advantage of the high thermal sensitivity and large optical penetration into tissues, scanning the subcutaneous temperature images in a minimally invasive way. Moreover *in-vivo* subcutaneous thermal videos opened the possibility to develop new diagnosis and control techniques with potential impact in existing biomedicine methods (Figure 17).[123]

Without using Ln^{3+} ions, Santos *et al.*[124] use the temporal decay temperature profiles monitored by Ag_2S IR nanothermometers to early-tumor diagnosis. The thermal transient thermometry can detect changes in tissues through changes in their thermal dynamics. Experimental data obtained in a murine model of melanoma reveal that at the early stages of tumor development (up to 7 days before it could be detected by optical inspection, Figure 18) and evident differences between the thermal relaxation dynamics of the tumoral tissue and a healthy area. The same group used NIR emitting PbS/CdS/ZnS QDs as deep tissue nanothermometers to discriminate between the ischemic and inflammatory phases (that occur after artery ligation), using exclusively thermal transient thermometry. The authors distinguish between the ischemic and the

healthy tissues by distinct temporal decays of the NIR luminescence. Furthermore the QDs were used for time monitoring the revascularization of tissues after temporal restriction of blood supply.[124]

5.2. Quantifying the materials properties through luminescence thermometry

Piñol *et al.* developed magnetic and thermometric NPs composed of γ-Fe_2O_3 superparamagnetic NPs recovered with Eu^{3+} and Tb^{3+} complexes and further polymeric layers to render aqueous stability.[126] The thermometer presents a high relative thermal sensitivity (5.8 %·K^{-1}) and low temperature uncertainty (0.5 K), whereas the NP demonstrated a relatively small heat capacitance. Taking advantage of the physical contact between the thermometer and the nanoheaters, the particles reveal the existence of an unexpected temperature gradient between nanoheaters and surrounding media (for $t > 10$ s) and relatively low heat powers (10^{-16} W per heater). Moreover, the continuous temperature monitoring with high time resolution allows the observation of previously undisclosed changes during the first few seconds ($t < 10$ s) of heating by an alternated magnetic field.[126] This work opened intriguing possibilities in studies of the heat flow at the nanoscale and triggered the experimental study of heat transfer processes occurring at sub-micrometric scales.

In a recent work, Baral *et al.*[227] measured the local temperature of an optically excited gold nanostructure combining near-field microscopy with Er^{3+} photoluminescence thermometry (in downshifting). The thermal images present spatial resolution limited only by the near-field scanning optical microscopy (SNOM) cantilever tip aperture (200 nm) being able to determine the actual local temperature from optically excited nanostructures, with temperature uncertainty near 1K and temporal resolution of 130 ms (still out of the sub-micrometer, sub-millisecond region, not covered so far by any example). The SNOM aperture tip can simultaneously be employed used to collect the Er^{3+} emission from a large illumination area where the steady-state thermal profile of an optically excited nanoparticle cluster is imaged. The steady-state thermal profiles from different sized clusters of 40 nm gold NPs show that the maximum temperature for the cluster scales with the size of the nanoparticle cluster. The technique allows to experimentally access the collective heating from a two-dimensional array of NPs that increases the total temperature increment and scales with cluster size.

Using Yb^{3+}/Er^{3+}-doped $NaYF_4$ nanocrystals of distinct sizes suspended in organic and inorganic solvents, Brites *et al.* use upconversion thermometry to measure the instantaneous Brownian velocity of the suspended nanocrystals.[128] A temperature step is imposed to a container and the real-time temperature monitoring by upconversion thermometry was used to calculate the time delay measured at distinct traveled distances, thus estimating the Brownian velocity of the nanocrystals for distinct volume fractions, solvents and nanoparticle sizes, Figure 19. The unique controlled size and high brightness of the nanocrystals enabled the coverage of a wide range of volume fraction values,[128] demonstrating that upconversion thermometry can be used to estimate basic parameters such as the convective heat transfer coefficient of the suspensions.

Guided by the same general purpose of evaluate the material's properties trough luminescence thermometry, the thermal conductivity of mesoporous SiO_2 and TiO_2 nanofilms was calculated using the luminescent temperature readout of Eu^{3+}/Tb^{3+}-codoped organic-inorganic hybrid probes.[129] Using first a 980 nm laser beam to promote the plasmonic heating of the nanostructures, the temperature decay after the heating beam turning off was followed by luminescence thermometry to further calculate the thermal conductivity of the nanolayers. The authors demonstrate that the reported non-contact and non-destructive strategy is able to estimate the nanolayers' thermal conductivity in accordance with the values reported for similar nanostructures using evasive electrical methods Figure 20.[129] The thermal conductivity of an AlGaN:Er^{3+} film was also recently evaluated using luminescence thermometry.[228] The authors positioned an Au micro disk over a AlGaN:Er^{3+} film deposited on a silicon substrate. Upon continuous 532 nm laser irradiation (power density of 6×10^9 $W\cdot m^{-2}$) the Au microdisks has a temperature increase of ~ 20 K. By temporal-modulating of the 532 nm laser intensity the authors induce a temperature increase followed by the temperature relaxation to the room-temperature which is monitored by the luminescence decay of $^2H_{11/2}\rightarrow{}^4I_{15/2}$ and the $^4S_{3/2}\rightarrow{}^4I_{15/2}$ transitions. The temperature is calculated using the ratio of the intensity decay curves and thus the heat-transfer dynamics was mapped with spatial resolution bellow 100 nm in the microsecond range. This work is able to follow the cooling of a single gold micro disk and to measure the rate of heat dissipation to the environment, directly calculating the absolute thermal conductivity of the AlGaN:Er^{3+} film (1.7 $W\cdot m^{-1}\cdot K^{-1}$) in agreement with the literature values.[228]

The thermal resistance of $KLuWO_4$:Tm^{3+}/Ho^{3+} NPs was also recently estimated using a fully noncontact approach through upconversion thermometry.[130] The thermal resistance of powder

NPs in contact with air was computed from the instantaneous temperature profiles and it was found to be of the same order of magnitude of that expected for interfacial thermal resistance Si nanorods and Si-based heterostructured nanowires.[130]

5.3. Exploring new strategies to enhance the thermal sensitivity

It is well known that temperature increase causes, in general, a loss in the light emission intensity that is known as thermal quenching, that limits the application of luminescent materials at higher temperatures. The thermal quenching is attributed to non-radiative relaxation pathways that are thermally activated because the material's atomic vibrations (phonons) are heightened with the temperature increase.

For NPs, however, there is a quenching channel, the so-called energy migration-induced surface quenching, that does not exist in their bulk counterparts. Recently, Cui *et al.*[229] demonstrated that the energy migration-induced surface quenching in Yb^{3+}-doped NPs can be suppressed by increasing temperature, resulting in an uncommon luminescence thermal enhancement. A mechanism based on the effect of thermal lattice expansion on Yb^{3+}-mediated energy migration is proposed to be beyond that unusual effect. Furthermore, since 2015 it was understood that the thermal effects on the light emission of UCNPs is a size-dependent phenomenon. Systematic studies on emission intensity of UCNPs upon distinct temperatures were performed by Li *et al.*[230, 231] and Shao *et al.*.[232, 233] The authors show that at higher temperatures (*e.g.* 300-500 K) whereas the emission intensity is enhanced for particles smaller than a critical size (*e.g.* 20–30 nm), it is quenched for bigger particles. This effect was used to control of NPs' emission color *via* modulation of the irradiation laser power or directly varying the temperature (through complex heating systems).[230, 231, 233] Although several models were advanced to explain these intriguing thermal effects, a recent explanation purposed by Zhou *et al.*[225] is being discussed in the literature. The authors observed an approximately 2000-fold enhancement in blue emission for 9.7 nm Yb^{3+}/Tm^{3+}-codoped UCNPs at 453 K, justifying their observations by a phonon-assisted energy transfer from sensitizers to activators, populating up the intermediate excited state of the UC process. The authors ascribed the phonon to existence of an oxygen moiety chelating Yb^{3+} ions, [Yb···O], present in the NPs due to the chelation Yb^{3+} ions at the nanoparticle's surface by carboxylic groups (of the capping molecules). A physical mechanism to fully explain this surface mechanism remains, however, absent.[234]

This new design principle opens the possibility to design novel size-dependent thermal probes that, using two emitting centers, can present higher performance in comparison to the existing ones. We notice that single-center thermometers on Boltzmann equation cannot benefit from the thermal enhancement effect in terms of relative sensitivity, however the minimum achievable temperature uncertainty can be reduced because the relative uncertainty $\delta\Delta/\Delta$ will be lower for small particles at higher temperatures. Moreover, its primary nature can be used to determine the absolute temperature of the nanoparticle despite the thermal enhancement or quenching effect be active. We can foresee that multi-center UC nanothermometers will have its thermal sensitivity increased from the current $1–3\%\cdot K^{-1}$ to values on the order of $5–10\%\cdot K^{-1}$ just by taking the ratio between thermally enhanced and thermally quenched emissions.

Martinez *et al.*[148] described a electrothermal device built by the assembly of nanocomposite transparent films combining a PMMA matrix and a percolating network of Ag nanowires[235, 236] covered by UCNPs of distinct sizes and compositions. The devices are excellent platforms to thermally fine-tune the particles' emission intensity and the NPs' local temperature and, thus, the emission color is easily controlled through the heat dissipation in the electrothermal device (by simply applying different DC voltages) providing a guide to fabricate innovative and versatile multichromatic upconversion nanostructures whose spectral emission can be externally adjusted by electrothermal control. From thermometric point of view, the devices incorporating Er^{3+}-doped NPs are inherently primary thermometers and the particle's local temperature can be accessed directly, using the intensity ratio of the green emission bands ($^2H_{11/2}\rightarrow{}^4I_{15/2}/{}^4S_{3/2}\rightarrow{}^4I_{15/2}$). For the Er^{3+}-doped NPs, irrespectively of thermal enhancement (diameter lower than 20 nm) or quenching (diameter higher than 20 nm), the intensity ratio increases with heating and the temperature calculated trough Eq.12 is consistent with the temperature probed by a thermocouple. Devices composed of small and large NPs containing distinct doping Ln^{3+} allow to estimate the temperature using the primary thermometer based on the green bands of Er^{3+}. The calculated temperature values were used to calibrate the secondary thermometer defined using a mixture of thermally enhanced and thermally quenched emission lines resulting a relative thermal sensitivity of about $6\ \%\cdot K^{-1}$.

https://doi.org/10.1002/adom.201801239

7. Summary and perspectives

The field of luminescence thermometry is growing intensively showing significant breakthroughs in sensing, imaging, diagnostics and therapy, among other areas. This interest has been mostly encouraged because many current technological demands in areas such as micro and nanoelectronics, photonics, micro and nanofluidics, and nanomedicine have reached a point such the use of conventional contact thermometers (liquid-filled and bimetallic thermometers, thermocouples, pyrometers, and thermistors) are not able to make measurements when spatial resolution decreases to the submicron scale. This limitation of conventional thermometers for small systems have spurred the development of luminescent micro and nanothermometers, a research topic leaving its inflationary epoch accounting nowadays for more than 2.5 % of the total publications in luminescence materials. Moreover, and from an industrial point of view, this predicted miniaturization is expected to bring to the market new nanoscale thermal probes. Despite the recently developed luminescent nanothermometers are radically more sophisticated encompassing complex synthesis procedures, the fundamental problems and the applications that are being addressed are analogous to those reported in the field's infancy: the understanding of heat transfer and energy transfer mechanisms, the optimization of temperature readout and the developing of efficient and cost-effective sensors for front-edge medical and engineering tools.

Among the distinct emitting centers used in luminescence thermometry, including proteins nucleic acids, and other biomolecules, thermosresponsive polymers, organic dyes and QDs, many Ln^{3+}-based luminescent thermometers have been reported, essentially in the last decade. Systems comprise molecular complexes, MOFs, polymers and organic-inorganic hybrids, multifunctional heater-thermometer nanoplatforms, and UC, DC, and DS NPs. This review describes the implementation of these Ln^{3+}-based phosphors as ratiometric thermometers in diverse applications, with focus on what the authors believe that will be the emergent new research areas in this fascinating research field: the use of luminescence thermometry for thermal imaging, early tumor detection and as a tool for unveil properties of the thermometers themselves or of their local surroundings.

Finally, to become a consolidated subject and not a temporary fashion, the research on luminescent thermometry must settle down as a strong node of fertile interactions among disparate communities, such as chemists, physicists, engineers, theoreticians, biologists, and physicians. The

https://doi.org/10.1002/adom.201801239

cross-fertilization of ideas and experiences at these interfaces will certainly induce important and exciting breakthroughs in future years.

Acknowledgements

Financial support of Fundação para a Ciência e a Tecnologia (FCT) (PTDC/CTM-NAN/4647/2014 and POCI-01-0145-FEDER-016687). This work was partially developed in the scope of the project CICECO − Aveiro Institute of Materials (Ref. FCT UID/CTM/50011/2013), financed by Portuguese funds through FCT/MEC and when applicable co-financed by FEDER under the PT2020 Partnership Agreement. The authors acknowledge Prof. Ricardo Longo (Universidade Federal de Pernambuco, Brazil) for fruitful discussions about the impact of nanoparticle' size on the relative sensitivity of luminescent nanothermometers. SB acknowledges EC Marie Curie Initial Training Network LUMINET (316906) and the support of Professor Marco Bettinelli and Laboratory of Solid State Chemistry from University of Verona, Italy. CDSB thanks the grant financed by the SusPhotoSolutions project CENTRO-01-0145-FEDER-000005.

References

[1] R. P. Benedict, *Fundamentals of Temperature, Pressure and Flow Measurements*, John Wiley & Sons Ltd, New York **1977**.
[2] F. Reif, *Fundamentals of Statistical and Thermal Physics*, McGraw-Hill, New York **1965**.
[3] M. Hartmann, *Contemp. Phys.* **2006**, *47*, 89.
[4] S. W. Allison, G. T. Gillies, *Rev. Sci. Instrum.* **1997**, *68*, 2615.
[5] P. R. N. Childs, J. R. Greenwood, C. A. Long, *Rev. Sci. Instrum.* **2000**, *71*, 2959.
[6] A. H. Khalid, K. Kontis, *Sensors-Basel* **2008**, *8*, 5673.
[7] O. S. Wolfbeis, *Adv. Mater.* **2008**, *20*, 3759.
[8] K. M. McCabe, M. Hernandez, *Pediatr. Res.* **2010**, *67*, 469.
[9] D. Jaque, L. M. Maestro, B. Del Rosal, P. Haro-Gonzalez, A. Benayas, J. Plaza, E. M. Rodríguez, J. G. Solé, *Nanoscale* **2014**, *6*, 9494.
[10] C. D. S. Brites, A. Millán, L. D. Carlos, in *Handbook on the Physics and Chemistry of Rare Earths*, Vol. 49 (Eds: J.-C. G. Bünzli, V. K. Pecharsky), Elsevier Science, B. V., Amsterdam **2016**, 339.
[11] S. Uchiyama, C. Gota, T. Tsuji, N. Inada, *Chem. Commun.* **2017**, *53*, 10976.
[12] *Temperature Sensors Market Analysis By Application (Automotive, Consumer Electronics, Environmental, Medical, Process Industries) and Segment Forecasts to 2020*, Vol. ISBN Code: 978-1-68038-495-6, **2015**.
[13] L. Michalski, K. Eckersdorf, J. Kucharski, J. McGhee, *Temperature Measurement*, John Wiley & Sons Ltd, West Sussex, England **2002**.
[14] S. Uchiyama, A. P. de Silva, K. Iwai, *J. Chem. Educ.* **2006**, *83*, 720.
[15] C. D. S. Brites, P. P. Lima, N. J. O. Silva, A. Millán, V. S. Amaral, F. Palacio, L. D. Carlos, *Adv. Mater.* **2010**, *22*, 4499.
[16] D. Jaque, F. Vetrone, *Nanoscale* **2012**, *4*, 4301.

[17] C. D. S. Brites, P. P. Lima, N. J. O. Silva, A. Millán, V. S. Amaral, F. Palacio, L. D. Carlos, *Nanoscale* **2012**, *4*, 4799.
[18] X. D. Wang, O. S. Wolfbeis, R. J. Meier, *Chem. Soc. Rev.* **2013**, *42*, 7834.
[19] M. D. Dramićanin, *Methods Appl. Fluoresc.* **2016**, *4*, 042001.
[20] S. S. Laha, A. R. Naik, E. R. Kuhn, M. Alvarez, A. Sujkowski, R. J. Wessells, B. P. Jena, *Nano Lett.* **2017**, *17*, 1262.
[21] M. Quintanilla, L. M. Liz-Marzan, *Nano Today* **2018**, *19*, 126.
[22] Y. Yue, X. Wang, *Nano Rev.* **2012**, *3*, 11586.
[23] S. Uchiyama, N. Kawai, A. P. de Silva, K. Iwai, *J. Am. Chem. Soc.* **2004**, *126*, 3032.
[24] S. Uchiyama, Y. Matsumura, A. P. de Silva, K. Iwai, *Anal. Chem.* **2003**, *75*, 5926.
[25] K. Okabe, N. Inada, C. Gota, Y. Harada, T. Funatsu, S. Uchiyama, *Nat. Commun.* **2012**, *3*, 705.
[26] J. S. Donner, S. A. Thompson, M. P. Kreuzer, G. Baffou, R. Quidant, *Nano Lett.* **2012**, *12*, 2107.
[27] P. Löw, B. Kim, N. Takama, C. Bergaud, *Small* **2008**, *4*, 908.
[28] G. Yang, X. Liu, J. Feng, S. Li, Y. Li, in *Thermometry at the nanoscale: techniques and selected applications*, Vol. 38 (Eds: L. D. Carlos, F. Palacio), The Royal Society of Chemistry, **2016**, 167.
[29] C. Paviolo, A. H. Clayton, S. L. McArthur, P. R. Stoddart, *J. Microsc.* **2013**, *250*, 179.
[30] J. Lee, A. O. Govorov, N. A. Kotov, *Angew. Chem.-Int. Edit.* **2005**, *44*, 7439.
[31] S. Kalytchuk, O. Zhovtiuk, S. V. Kershaw, R. Zboril, A. L. Rogach, *Small* **2016**, *12*, 466.
[32] M. Back, E. Trave, J. Ueda, S. Tanabe, *Chem. Matter.* **2016**, *28*, 8347−8356.
[33] C. Pietsch, U. S. Schubert, R. Hoogenboom, *Chem. Commun.* **2011**, *47*, 8750.
[34] V. R. de la Rosa, P. Woisel, R. Hoogenboom, *Mater. Today* **2016**, *19*, 44.
[35] S. Li, K. Zhang, J. M. Yang, L. W. Lin, H. Yang, *Nano Lett.* **2007**, *7*, 3102.
[36] P. Haro-Gonzalez, W. T. Ramsay, L. Martinez Maestro, B. del Rosal, K. Santacruz-Gomez, M. C. Iglesias de la Cruz, F. Sanz-Rodríguez, J. Y. Chooi, P. Rodríguez Sevilla, M. Bettinelli, D. Choudhury, A. K. Kar, J. G. Solé, D. Jaque, L. Paterson, *Small* **2013**, *9*, 2162.
[37] S. J. Cho, D. Maysinger, M. Jain, B. Roder, S. Hackbarth, F. M. Winnik, *Langmuir* **2007**, *23*, 1974.
[38] A. Gnach, T. Lipinski, A. Bednarkiewicz, J. Rybka, J. A. Capobianco, *Chem. Soc. Rev.* **2015**, *44*, 1561.
[39] L. M. Maestro, P. Haro-González, M. C. Iglesias de la Cruz, F. Sanz Rodríguez, A. Juarranz, J. G. Solé, D. Jaque, *Nanomedicine* **2013**, *8*, 379.
[40] J. C. G. Bünzli, S. V. Eliseeva, *Chem. Sci.* **2013**, *4*, 1939.
[41] J.-C. G. Bünzli, *Coordin. Chem. Rev.* **2015**, *293*, 19.
[42] L. D. Carlos, R. A. S. Ferreira, V. de Zea Bermudez, S. J. L. Ribeiro, *Adv. Mater.* **2009**, *21*, 509.
[43] K. Binnemans, *Chem. Rev.* **2009**, *109*, 4283.
[44] J.-C. G. Bünzli, *Chem. Rev.* **2010**, *110*, 2729.
[45] J. Feng, H. J. Zhang, *Chem. Soc. Rev.* **2013**, *42*, 387.
[46] G. Y. Chen, C. H. Yang, P. N. Prasad, *Accounts Chem. Res.* **2013**, *46*, 1474.
[47] H. Peng, M. I. Stich, J. Yu, L. N. Sun, L. H. Fischer, O. S. Wolfbeis, *Adv. Mater.* **2010**, *22*, 716.
[48] Z. Wang, D. Ananias, A. Carné-Sánchez, C. D. S. Brites, I. Inhar, D. Maspoch, J. Rocha, L. D. Carlos, *Adv. Funct. Mater.* **2015**, *25*, 2824.
[49] Y. Cui, F. Zhu, B. Chen, G. Qian, *Chem. Commun.* **2015**, *51*, 7420.
[50] A. Cadiau, C. D. S. Brites, P. M. F. J. Costa, R. A. S. Ferreira, J. Rocha, L. D. Carlos, *ACS Nano* **2013**, *7*, 7213.
[51] J. Rocha, C. D. S. Brites, L. D. Carlos, *Chem. Eur. J.* **2016**, *22*, 14782.
[52] S. Arai, Ferdinandus, S. Takeoka, S. Ishiwata, H. Sato, M. Suzuki, *Analyst* **2015**, *140*, 7534.
[53] E. N. Cerón, D. H. Ortgies, B. del Rosal, F. Ren, A. Benayas, F. Vetrone, D. Ma, F. Sanz-Rodríguez, J. G. Solé, D. Jaque, E. M. Rodríguez, *Adv. Mater.* **2015**, *27*, 4781.
[54] C. D. S. Brites, P. P. Lima, N. J. O. Silva, A. Millán, V. S. Amaral, F. Palacio, L. D. Carlos, *Nanoscale* **2013**, *5*, 7572.

[55] G. Jalani, R. Naccache, D. H. Rosenzweig, L. Haglund, F. Vetrone, M. Cerruti, *J. Am. Chem. Soc.* **2016**, *138*, 1078.
[56] M. L. Debasu, C. D. S. Brites, S. Balabhadra, H. Oliveira, J. Rocha, L. D. Carlos, *ChemNanoMat* **2016**, *2*, 520.
[57] X. Zhu, W. Feng, J. Chang, Y.-W. Tan, J. Li, M. Chen, Y. Sun, F. Li, *Nat. Commun.* **2016**, *7*, 10437.
[58] O. A. Savchuk, P. Haro-González, J. J. Carvajal, D. Jaque, J. Massons, M. Aguiló, F. Diaz, *Nanoscale* **2014**, *6*, 9727.
[59] M. Bettinelli, L. D. Carlos, X. Liu, *Phys. Today* **2015**, *68*, 38.
[60] V. Lojpur, M. G. Nikolić, M. D. Dramićanin, *J. Appl. Phys.* **2014**, *115*, 203106.
[61] F. Vetrone, R. Naccache, A. Zamarron, Á. J. de la Fuente, F. Sanz-Rodriguez, L. M. Maestro, E. M. Rodriguez, D. Jaque, J. G. Solé, J. A. Capobianco, *ACS Nano* **2010**, *4*, 3254.
[62] T. V. Gavrilović, D. J. Jovanović, V. Lojpur, M. D. Dramićanin, *Sci. Rep.* **2014**, *4*, 4209.
[63] S. Balabhadra, M. L. Debasu, C. D. Brites, L. A. Nunes, O. L. Malta, J. Rocha, M. Bettinelli, L. D. Carlos, *Nanoscale* **2015**, *7*, 17261.
[64] Ł. Marciniak, A. Bednarkiewicz, M. Stefanski, R. Tomala, D. Hreniak, W. Strek, *Phys. Chem. Chem. Phys.* **2015**, *17*, 24315.
[65] U. Rocha, K. U. Kumar, C. Jacinto, I. Villa, F. Sanz-Rodríguez, M. C. Iglesias de la Cruz, A. Juarranz, E. Carrasco, F. C. van Veggel, E. Bovero, J. G. Solé, D. Jaque, *Small* **2014**, *10*, 1141.
[66] A. Benayas, B. del Rosal, A. Perez-Delgado, K. Santacruz-Gomez, D. Jaque, G. A. Hirata, F. Vetrone, *Adv. Opt. Mater.* **2015**, *3*, 687.
[67] A. L. Heyes, *J. Lumin.* **2009**, *129*, 2004.
[68] J. B. Yu, L. N. Sun, H. S. Peng, M. I. J. Stich, *J. Mater. Chem.* **2010**, *20*, 6975.
[69] A. Rabhiou, J. Feist, A. Kempf, S. Skinner, A. Heyes, *Sens. Actuators A: Phys.* **2011**, *169*, 18.
[70] C. D. S. Brites, P. P. Lima, N. J. O. Silva, A. Millán, V. S. Amaral, F. Palacio, L. D. Carlos, *New J. Chem.* **2011**, *35*, 1177.
[71] L. H. Fischer, G. S. Harms, O. S. Wolfbeis, *Angew. Chem.-Int. Edit.* **2011**, *50*, 4546.
[72] A. L. Heyes, A. Rabhiou, J. P. Feist, A. Kempf, *AIP Conf. Proc.* **2013**, *1552*, 891.
[73] D. Jaque, B. del Rosal, E. M. Rodriguez, L. M. Maestro, P. Haro-Gonzalez, J. G. Solé, *Nanomedicine* **2014**, *9*, 1047.
[74] C. Wang, F. Zhang, in *Photon Upconversion Nanomaterials*, Vol. 46 (Ed: F. Zhang), Springer, Berlin **2015**, 343.
[75] X. F. Wang, Q. Liu, Y. Y. Bu, C. S. Liu, T. Liu, X. H. Yan, *RSC Adv.* **2015**, *5*, 86219.
[76] A. Millán, L. D. Carlos, C. D. S. Brites, N. J. O. Silva, R. Piñol, F. Palacio, in *Thermometry at the Nanoscale: Techniques and Selected Applications*, Vol. 38 (Eds: L. D. Carlos, F. Palacio), The Royal Society of Chemistry, Oxfordshire **2016**, 237.
[77] M. Quintanilla, A. Benayas, R. Naccache, F. Vetrone, in *Thermometry at the nanoscale: techniques and selected applications*, Vol. 38 (Eds: L. D. Carlos, F. Palacio), The Royal Society of Chemistry, Oxfordshire **2016**, 124.
[78] H. Zhou, M. Sharma, O. Berezin, D. Zuckerman, M. Y. Berezin, *ChemPhysChem* **2016**, *17*, 27.
[79] E. Hemmer, P. Acosta-Mora, J. Mendez-Ramos, S. Fischer, *J. Mater. Chem. B* **2017**, *5*, 4365.
[80] B. Liu, C. X. Li, P. P. Yang, Z. Y. Hou, J. Lin, *Adv. Mater.* **2017**, *29*, 1605434.
[81] B. del Rosal, E. Ximendes, U. Rocha, D. Jaque, *Adv. Opt. Mater.* **2017**, *5*, 1600508.
[82] Y. Cheng, Y. Gao, H. Lin, F. Huang, Y. Wang, *J. Mater. Chem. C* **2018**, *6*, 7462.
[83] L. D. Carlos, F. Palacio, *Thermometry at the Nanoscale: Techniques and Selected Applications*, Royal Society of Chemistry, Oxfordshire **2016**.
[84] M. Dramićanin, *Luminescence Thermometry: Methods, Materials, and Applications*, Woodhead Publishing, **2018**.

[85] P. Neubert, Method and apparatus for recording the temperatures of hot bodies. *US2085508 A*, 1937.
[86] P. Neubert, Device for indicating the temperature distribution of hot bodies. *US2071471A*, 1937.
[87] F. Urbach, N. R. Nail, D. Pearlman, *J. Opt. Soc. Am.* **1949**, *39*, 1011.
[88] L. C. Bradley, *Rev. Sci. Instrum.* **1953**, *24*, 219.
[89] R. N. Lawson, *Ann. NY Acad. Sci.* **1964**, *121*, 31.
[90] R. N. Lawson, L. L. Alt, *Can. Med. Assoc. J.* **1965**, *92*, 255.
[91] H. Kusama, O. J. Sovers, T. Yoshioka, *Jpn. J. Appl. Phys.* **1976**, *15*, 2349.
[92] T. Samulski, P. N. Shrivastava, *Science* **1980**, *208*, 193.
[93] T. V. Samulski, P. T. Chopping, B. Haas, *Phys. Med. Biol.* **1982**, *27*, 107.
[94] P. Kolodner, J. A. Tyson, *Appl. Phys. Lett.* **1983**, *42*, 117.
[95] P. Kolodner, A. Katzir, N. Hartsough, *Appl. Phys. Lett.* **1983**, *42*, 749.
[96] P. Kolodner, J. A. Tyson, *Appl. Phys. Lett.* **1982**, *40*, 782.
[97] K. A. Wickersheim, R. B. Alves, *Ind. Res. Dev.* **1979**, *21*, 82.
[98] K. A. Wickersheim, M. H. Sun, *J. Microw. Power Electromagn. Energy* **1987**, *22*, 85.
[99] *LumaSense Technologies*, https://www.lumasenseinc.com/EN/products/technology-overview/our-technologies/fluoroptic/fluoroptic-temperature-measurement.html (June 2018).
[100] E. Schena, D. Tosi, P. Saccomandi, E. Lewis, T. Kim, *Sensors-Basel* **2016**, *16*, 1144.
[101] S. Musolino, E. P. Schartner, G. Tsiminis, A. Salem, T. M. Monro, M. R. Hutchinson, *Biomed. Opt. Express* **2016**, *7*, 3069.
[102] S. P. Wang, S. Westcott, W. Chen, *J. Phys. Chem. B* **2002**, *106*, 11203.
[103] M. A. R. C. Alencar, G. S. Maciel, C. B. de Araújo, A. Patra, *Appl. Phys. Lett.* **2004**, *84*, 4753.
[104] V. Tikhomirov, K. Driesen, V. Rodriguez, P. Gredin, M. Mortier, V. Moshchalkov, *Opt. Express* **2009**, *17*, 11794.
[105] D. Wawrzynczyk, A. Bednarkiewicz, M. Nyk, W. Strek, M. Samoc, *Nanoscale* **2012**, *4*, 6959.
[106] F. Vetrone, R. Naccache, Á. J. de la Fuente, F. Sanz-Rodriguez, A. Blazquez-Castro, E. M. Rodriguez, D. Jaque, J. G. Solé, J. A. Capobianco, *Nanoscale* **2010**, *2*, 495.
[107] Y. J. Cui, H. Xu, Y. F. Yue, Z. Y. Guo, J. C. Yu, Z. X. Chen, J. K. Gao, Y. Yang, G. D. Qian, B. L. Chen, *J. Am. Chem. Soc.* **2012**, *134*, 3979.
[108] Q. Q. Zhan, J. Qian, H. J. Liang, G. Somesfalean, D. Wang, S. L. He, Z. G. Zhang, S. Andersson-Engels, *ACS Nano* **2011**, *5*, 3744.
[109] B. Dong, B. S. Cao, Y. Y. He, Z. Liu, Z. P. Li, Z. Q. Feng, *Adv. Mater.* **2012**, *24*, 1987.
[110] M. I. J. Stich, L. H. Fischer, O. S. Wolfbeis, *Chem. Soc. Rev.* **2010**, *39*, 3102.
[111] M. Alden, A. Omrane, M. Richter, G. Sarner, *Prog. Energ. Combust.* **2011**, *37*, 422.
[112] J. Brübach, C. Pflitsch, A. Dreizler, B. Atakan, *Prog. Energy Combust. Sci.* **2013**, *39*, 37.
[113] J. M. Hu, S. Y. Liu, *Macromolecules* **2010**, *43*, 8315.
[114] R. A. S. Ferreira, C. D. S. Brites, C. M. S. Vicente, P. P. Lima, A. R. N. Bastos, P. G. Marques, M. Hiltunen, L. D. Carlos, P. S. André, *Laser Photonics Rev.* **2013**, *7*, 1027.
[115] R. Y. He, J. R. V. de Aldana, G. L. Pedrola, F. Chen, D. Jaque, *Opt. Express* **2016**, *24*, 16156.
[116] C. D. S. Brites, P. P. Lima, N. J. O. Silva, A. Millán, V. S. Amaral, F. Palacio, L. D. Carlos, *Front. Chem.* **2013**, *1*, 9.
[117] O. A. Savchuk, J. J. Carvajal, J. Massons, C. Cascales, M. Aguiló, F. Díaz, *Sens. Actuator A-Phys.* **2016**, *250*, 87.
[118] R. G. Geitenbeek, A. E. Nieuwelink, T. S. Jacobs, B. B. V. Salzmann, J. Goetze, A. Meijerink, B. M. Weckhuysen, *ACS Catal.* **2018**, *8*, 2397.
[119] Ž. Antić, M. D. Dramićanin, K. Prashanthi, D. Jovanović, S. Kuzman, T. Thundat, *Adv. Mater.* **2016**, *28*, 7745.
[120] C. Abram, B. Fond, F. Beyrau, *Prog. Energy Combust. Sci.* **2018**, *64*, 93.

[121] T. Miyagawa, T. Fujie, Ferdinandus, T. T. V. Doan, H. Sato, S. Takeoka, *ACS Appl. Mater. Interfaces* **2016**, *8*, 33377.
[122] Ferdinandus, S. Arai, S. Takeoka, S. Ishiwata, M. Suzuki, H. Sato, *ACS Sensors* **2016**, *1*, 1222.
[123] E. C. Ximendes, U. Rocha, T. O. Sales, N. Fernández, F. Sanz‐Rodríguez, I. R. Martín, C. Jacinto, D. Jaque, *Adv. Funct. Mater.* **2017**, 1702249.
[124] E. C. Ximendes, U. Rocha, B. del Rosal, A. Vaquero, F. Sanz‐Rodríguez, L. Monge, F. Ren, F. Vetrone, D. Ma, J. García‐Solé, *Adv. Healthcare Mater.* **2017**, *6*, 1601195.
[125] H. D. A. Santos, E. C. Ximendes, M. C. I.-d. l. Cruz, I. Chaves-Coira, B. d. Rosal, C. Jacinto, L. Monge, I. Rubia-Rodríguez, D. Ortega, S. Mateos, J. G. Solé, D. Jaque, N. Fernández, *Adv. Functional Mater.* **2018**, in press.
[126] R. Piñol, C. D. S. Brites, R. Bustamante, A. Martínez, N. J. O. Silva, J. L. Murillo, R. Cases, J. Carrey, C. Estepa, C. Sosa, F. Palacio, L. D. Carlos, A. Millán, *ACS Nano* **2015**, *9*, 3134.
[127] E. C. Ximendes, W. Q. Santos, U. Rocha, U. K. Kagola, F. Sanz-Rodriguez, N. Fernandez, A. D. Gouveia-Neto, D. Bravo, A. M. Domingo, B. del Rosal, C. D. S. Brites, L. D. Carlos, D. Jaque, C. Jacinto, *Nano Lett.* **2016**, *16*, 1695.
[128] C. D. Brites, X. Xie, M. L. Debasu, X. Qin, R. Chen, W. Huang, J. Rocha, X. Liu, L. D. Carlos, *Nat. Nanotechn.* **2016**, *11*, 851.
[129] C. D. S. Brites, M. C. Fuertes, P. C. Angelomé, E. D. Martínez, P. P. Lima, G. J. A. A. Soler-Illia, L. D. Carlos, *Nano Lett.* **2017**, *17*, 4746.
[130] O. A. Savchuk, J. J. Carvajal, C. D. S. Brites, L. D. Carlos, M. Aguilo, F. Diaz, *Nanoscale* **2018**, *10*, 6602.
[131] J. Christofferson, K. Maize, Y. Ezzahri, J. Shabani, X. Wang, A. Shakouri, *J. Electron. Packaging* **2008**, *130*, 041101.
[132] T. J. Quinn, *Temperature*, Elsevier Science, **2013**.
[133] J. Fischer, S. Gerasimov, K. D. Hill, G. Machin, M. R. Moldover, L. Pitre, P. Steur, M. Stock, O. Tamura, H. Ugur, D. R. White, I. Yang, J. Zhang, *Int. J. Thermophys.* **2007**, *28*, 1753.
[134] B. Fellmuth, J. Fischer, G. Machin, S. Picard, P. P. M. Steur, O. Tamura, D. R. White, H. Yoon, *Phil. Trans. R. Soc. A.* **2016**, *374*, 20150037.
[135] D. Pugh-Thomas, B. M. Walsh, M. C. Gupta, *Nanotechnology* **2011**, *22*, 185503.
[136] A. M. P. Botas, C. D. S. Brites, J. Wu, U. Kortshagen, R. N. Pereira, L. D. Carlos, R. A. S. Ferreira, *Part. Part. Syst. Charact.* **2016**, *33*, 740.
[137] A. S. Souza, L. A. O. Nunes, I. G. N. Silva, F. A. M. Oliveira, L. L. da Luz, H. F. Brito, M. C. F. C. Felinto, R. A. S. Ferreira, S. A. Junior, L. D. Carlos, O. L. Malta, *Nanoscale* **2016**, *8*, 5327.
[138] S. Balabhadra, M. L. Debasu, C. D. S. Brites, R. A. S. Ferreira, L. D. Carlos, *J. Phys. Chem. C* **2017**, *121*, 13962.
[139] S. F. Collins, G. W. Baxter, S. A. Wade, T. Sun, K. T. V. Grattan, Z. Y. Zhang, A. W. Palmer, *J. Appl. Phys.* **1998**, *84*, 4649.
[140] R. Alicki, D. M. Leitner, *J. Phys. Chem. B* **2015**, *119*, 9000.
[141] G. Toth, I. Apellaniz, *J. Phys A-Math. Theor.* **2014**, *47*.
[142] A. A. Alaulamie, *Nanoscale Temperature Measurement of Phase Transition in Water Using Novel Optical Thermometry Techniques*, Ph.D. thesis, College of Arts and Sciences of Ohio University, **2017**.
[143] S. Collins, G. Baxter, S. Wade, T. Sun, K. Grattan, Z. Zhang, A. Palmer, *J. Appl. Phys.* **1998**, *84*, 4649.
[144] S. A. Wade, S. F. Collins, G. W. Baxter, *J. Appl. Phys.* **2003**, *94*, 4743.
[145] M. D. Shinn, W. A. Sibley, M. G. Drexhage, R. N. Brown, *Phys. Rev. B* **1983**, *27*, 6635.
[146] S. F. León-Luis, U. R. Rodríguez-Mendoza, P. Haro-González, I. R. Martín, V. Lavín, *Sensor Actuat. B-Chem.* **2012**, *174*, 176.
[147] A. H. Khalid, K. Kontis, *Meas. Sci. Technol.* **2009**, *20*, 025305.

[148] E. D. Martínez, C. D. S. Brites, L. D. Carlos, A. F. García-Flores, R. R. Urbano, C. Rettori, **2018**, submitted.
[149] M. T. Carlson, A. Khan, H. H. Richardson, *Nano Lett.* **2011**, *11*, 1061.
[150] M. L. Debasu, D. Ananias, I. Pastoriza-Santos, L. M. Liz-Marzán, J. Rocha, L. D. Carlos, *Adv. Mater.* **2013**, *25*, 4868.
[151] B. R. Judd, *Phys. Rev.* **1962**, *127*, 750.
[152] G. S. Ofelt, *J. Chem. Phys.* **1962**, *37*, 511.
[153] G. F. de Sá, O. L. Malta, C. de Mello Donegá, A. M. Simas, R. L. Longo, P. A. Santa-Cruz, E. F. da Silva, *Coord. Chem. Rev.* **2000**, *196*, 165.
[154] O. L. Malta, L. D. Carlos, *Quim. Nova* **2003**, *26*, 889.
[155] W. T. Carnall, H. Crosswhite, H. M. Crosswhite, *Energy Level Structure and Transition Probabilities in the Spectra of the Trivalent Lanthanides In LaF_3*, Argonne Nat. Lab. 78-XX-95 Rep., **1977**.
[156] C. Görller-Walrand, K. Binnemans, in *Handbook on the Physics and Chemistry of Rare Earths*, Vol. 25 (Eds: K. A. G. Jr., L. Eyring), North-Holland Publishers Amsterdam **1998**, 101.
[157] Y. M. Yang, C. Mi, F. Yu, X. Y. Su, C. F. Guo, G. Li, J. Zhang, L. L. Liu, Y. Z. Liu, X. D. Li, *Ceram. Int.* **2014**, *40*, 9875.
[158] Y. M. Yang, C. Mi, F. Y. Jiao, X. Y. Su, X. D. Li, L. L. Liu, J. Zhang, F. Yu, Y. Z. Liu, Y. H. Mai, *J. Am. Ceram. Soc.* **2014**, *97*, 1769.
[159] N. Rakov, G. S. Maciel, *J. Appl. Phys.* **2017**, *121*, 113103.
[160] B. Henderson, G. F. Imbusch, *Optical Spectroscopy of Inorganic Solids*, Oxford Science Publications **1989**.
[161] H. S. Peng, H. W. Song, B. J. Chen, J. W. Wang, S. Z. Lu, X. G. Kong, J. H. Zhang, *J. Chem. Phys.* **2003**, *118*, 3277.
[162] X. Wang, J. Zheng, Y. Xuan, X. Yan, *Opt. Express* **2013**, *21*, 21596.
[163] M. A. Hernandez-Rodriguez, A. D. Lozano-Gorrin, I. R. Martin, U. R. Rodriguez-Mendoza, V. Lavin, *Sensor Actuat. B-Chem.* **2018**, *255*, 970.
[164] A. R. Zanatta, D. Scoca, F. Alvarez, *Sci. Rep.-UK* **2017**, *7*, 14113.
[165] M. G. Lahoud, R. C. G. Frem, D. A. Galico, G. Bannach, M. M. Nolasco, R. A. S. Ferreira, L. D. Carlos, *J. Lumin.* **2016**, *170*, 357.
[166] V. K. Rai, S. B. Rai, *Appl. Phys. B-Lasers O* **2007**, *87*, 323.
[167] D. A. Gálico, I. O. Mazali, F. A. Sigoli, *J. Lumin.* **2017**, *192*, 224.
[168] S. Gharouel, L. Labrador-Páez, P. Haro-González, K. Horchani-Naifer, M. Férid, *J. Lumin.* **2018**.
[169] S. Sato, R. Yamaguchi, T. Nose, *Institute of Electronics, Information and Communication Engineers Journal C* **1989**, *J72-C2 (in Japanese)*, 906.
[170] M. Suzuki, V. Tseeb, K. Oyama, S. Ishiwata, *Biophys. J.* **2007**, *92*, L46.
[171] M. Hatanaka, Y. Hirai, Y. Kitagawa, T. Nakanishi, Y. Hasegawa, K. Morokuma, *Chem. Sci.* **2017**, *8*, 423.
[172] P. P. Lima, M. M. Nolasco, F. A. A. Paz, R. A. S. Ferreira, R. L. Longo, O. L. Malta, L. D. Carlos, *Chem. Mater.* **2013**, *25*, 586.
[173] K. Miyata, Y. Konno, T. Nakanishi, A. Kobayashi, M. Kato, K. Fushimi, Y. Hasegawa, *Angew. Chem.-Int. Edit.* **2013**, *52*, 6413.
[174] Y. Liu, G. D. Qian, Z. Y. Wang, M. Q. Wang, *Appl. Phys. Lett.* **2005**, *86*, 071907.
[175] M. Rodrigues, R. Piñol, G. Antorrena, C. D. S. Brites, N. J. O. Silva, J. L. Murillo, R. Cases, I. Díez, F. Palacio, N. Torras, J. A. Plaza, L. Pérez-García, L. D. Carlos, A. Millán, *Adv. Funct. Mater.* **2016**, *26*, 200.
[176] J. F. C. B. Ramalho, L. C. F. António, S. F. H. Correia, L. S. Fu, A. S. Pinho, C. D. S. Brites, L. D. Carlos, P. S. André, R. A. S. Ferreira, *Opt. Laser. Tech.* **2018**, *101*, 304.
[177] H. Furukawa, K. E. Cordova, M. O'Keeffe, O. M. Yaghi, *Science* **2013**, *341*, 974.
[178] J. Rocha, L. D. Carlos, F. A. A. Paz, D. Ananias, *Chem. Soc. Rev.* **2011**, *40*, 926.

[179] W. P. Lustig, S. Mukherjee, N. D. Rudd, A. V. Desai, J. Li, S. K. Ghosh, *Chem. Soc. Rev.* **2017**, *46*, 3242.
[180] B. Li, H. M. Wen, Y. J. Cui, W. Zhou, G. D. Qian, B. L. Chen, *Adv. Mater.* **2016**, *28*, 8819.
[181] X. Liu, S. Akerboom, M. de Jong, I. Mutikainen, S. Tanase, A. Meijerink, E. Bouwman, *Inorg. Chem.* **2015**, *54*, 11323.
[182] Y. J. Cui, W. F. Zou, R. J. Song, J. C. Yu, W. Q. Zhang, Y. Yang, G. D. Qian, *Chem. Commun.* **2014**, *50*, 719.
[183] W. Liu, L. J. Liu, Y. L. Wang, L. H. Chen, J. A. McLeod, L. J. Yang, J. Zhao, Z. Y. Liu, D. W. Juan, Z. F. Chai, T. E. Albrecht-Schmitt, G. K. Liu, S. Wang, *Chem-Eur. J.* **2016**, *22*, 11170.
[184] L. Li, Y. L. Zhu, X. H. Zhou, C. D. S. Brites, D. Ananias, Z. Lin, F. A. A. Paz, J. Rocha, W. Huang, L. D. Carlos, *Adv. Funct. Mater.* **2016**, *26*, 8677.
[185] N. Bloembergen, *Phys. Rev. Lett.* **1959**, *2*, 84.
[186] F. Auzel, *C.R. Acad. Sci. Paris* **1966**, *263*, 819.
[187] F. P. P. Ovsyankin V. V., *J. Exp. Theor. Phys.* **1966**, *3*, 322.
[188] L. Prodi, E. Rampazzo, F. Rastrelli, A. Speghini, N. Zaccheroni, *Chem. Soc. Rev.* **2015**, *44*, 4922.
[189] K. Nigoghossian, Y. Messaddeq, D. Boudreau, S. J. L. Ribeiro, *ACS Omega* **2017**, *2*, 2065.
[190] E. M. Rodrigues, D. A. Gálico, M. A. Lemes, J. Bettini, E. T. Neto, I. O. Mazali, M. Murugesu, F. A. Sigoli, *New J. Chem.* **2018**, *42*, 13393.
[191] R. G. Geitenbeek, P. T. Prins, W. Albrecht, A. van Blaaderen, B. M. Weckhuysen, A. Meijerink, *J. Phys. Chem. C* **2017**, *121*, 3503.
[192] C. D. S. Brites, K. Fiaczyk, J. F. C. B. Ramalho, M. Sojka, L. D. Carlos, E. Zych, *Adv. Opt. Mater.* **2018**, *6*.
[193] I. E. Kolesnikov, A. A. Kalinichev, M. A. Kurochkin, E. V. Golyeva, E. Y. Kolesnikov, A. V. Kurochkin, E. Lahderanta, M. D. Mikhailov, *Sci. Rep.-UK* **2017**, *7*.
[194] A. Sedlmeier, D. E. Achatz, L. H. Fischer, H. H. Gorris, O. S. Wolfbeis, *Nanoscale* **2012**, *4*, 7090.
[195] V. Lojpur, M. G. Nikolić, L. Mancic, O. Milosevic, M. D. Dramićanin, *Ceram. Int.* **2013**, *39*, 1129.
[196] N. N. Dong, M. Pedroni, F. Piccinelli, G. Conti, A. Sbarbati, J. E. Ramírez-Hernández, L. M. Maestro, M. C. Iglesias de la Cruz, F. Sanz-Rodríguez, A. Juarranz, F. Chen, F. Vetrone, J. A. Capobianco, J. G. Solé, M. Bettinelli, D. Jaque, A. Speghini, *ACS Nano* **2011**, *5*, 8665.
[197] B. Dong, R. N. Hua, B. S. Cao, Z. P. Li, Y. Y. He, Z. Y. Zhang, O. S. Wolfbeis, *Phys. Chem. Chem. Phys.* **2014**, *16*, 20009.
[198] Ł. Marciniak, K. Prorok, A. Bednarkiewicz, *J. Mater. Chem. C* **2017**, *5*, 7890.
[199] Ł. Marciniak, A. Bednarkiewicz, W. Strek, *Sens. Actuator B-Chem.* **2017**, *238*, 381.
[200] A. C. Brandão-Silva, M. A. Gomes, S. M. V. Novais, Z. S. Macedo, J. F. M. Avila, J. J. Rodrigues, M. A. R. C. Alencar, *J. Alloys Comp.* **2018**, *731*, 478.
[201] H. Suo, C. F. Guo, J. M. Zheng, B. Zhou, C. G. Ma, X. Q. Zhao, T. Li, P. Guo, E. M. Goldys, *ACS Appl. Mater. Inter.* **2016**, *8*, 30312.
[202] R. Marin, L. Labrador-Paéz, A. Skripka, P. Haro-González, A. Benayas, P. Canton, D. Jaque, F. Vetrone, *ACS Photonics* **2018**.
[203] F. Yang, A. Skripka, A. Benayas, X. Dong, H. Hong Sung, F. Ren, K. Oh Jung, X. Liu, F. Vetrone, D. Ma, *Adv. Funct. Mater.* **2018**, *28*, 1706235.
[204] S. Zhou, G. Jiang, X. Li, S. Jiang, X. Wei, Y. Chen, M. Yin, C. Duan, *Opt. Lett.* **2014**, *39*, 6687.
[205] S. H. Zheng, W. B. Chen, D. Z. Tan, J. J. Zhou, Q. B. Guo, W. Jiang, C. Xu, X. F. Liu, J. R. Qiu, *Nanoscale* **2014**, *6*, 5675.
[206] M. Xu, D. Chen, P. Huang, Z. Wan, Y. Zhou, Z. Ji, *J. Mater. Chem. C* **2016**, *4*, 6516.
[207] A. Pandey, V. K. Rai, *Appl. Phys. B* **2013**, 1.
[208] N. Ishiwada, S. Fujioka, T. Ueda, T. Yokomori, *Opt. Lett.* **2011**, *36*, 760.

[209] Ł. Marciniak, A. Bednarkiewicz, M. Stefanski, R. Tomala, D. Hreniak, W. Strek, *Phys. Chem. Chem. Phys.* **2015**, *17*, 24315.
[210] E. Hemmer, A. Benayas, F. Legare, F. Vetrone, *Nanoscale Horiz.* **2016**, *1*, 168.
[211] R. Weissleder, *Nat. Biotechnol.* **2001**, *19*, 316.
[212] A. M. Smith, M. C. Mancini, S. Nie, *Nat. Nanotech.* **2009**, *4*, 710.
[213] D. Jaque, C. Richard, B. Viana, K. Soga, X. Liu, J. García Solé, *Adv. Opt. Photon.* **2016**, *8*, 1.
[214] A. Skripka, A. Benayas, R. Marin, P. Canton, E. Hemmer, F. Vetrone, *Nanoscale* **2017**, *9*, 3079.
[215] Ł. Marciniak, K. Prorok, L. Frances-Soriano, J. Perez-Prieto, A. Bednarkiewicz, *Nanoscale* **2016**, *8*, 5037.
[216] L. Labrador-Páez, E. C. Ximendes, P. Rodriguez Sevilla, D. H. Ortgies, U. Rocha, C. Jacinto, E. Martín Rodríguez, P. Haro Gonzalez, D. Jaque Garcia, *Nanoscale* **2018**, 10.1039/C8NR02307G.
[217] F. Yang, A. Skripka, A. Benayas, X. K. Dong, S. H. Hong, F. Q. Ren, J. K. Oh, X. Y. Liu, F. Vetrone, D. L. Ma, *Adv Funct Mater* **2018**, *28*.
[218] Y. Huang, E. Hemmer, F. Rosei, F. Vetrone, *J. Phys. Chem. B* **2016**, *120*, 4992.
[219] J. Huang, B. He, Z. Cheng, L. Zhou, *J. Lumin.* **2015**, *160*, 254.
[220] R. Chen, V. D. Ta, F. Xiao, Q. Y. Zhang, H. D. Sun, *Small* **2013**, *9*, 1052.
[221] Q. B. Xiao, Y. F. Li, F. J. Li, M. X. Zhang, Z. J. Zhang, H. Z. Lin, *Nanoscale* **2014**, *6*, 10179.
[222] S. Rohani, M. Quintanilla, S. Tuccio, F. De Angelis, E. Cantelar, A. O. Govorov, L. Razzari, F. Vetrone, *Adv. Opt. Mater.* **2015**, *3*, 1606.
[223] Z. Wang, P. Zhang, Q. Yuan, X. Xu, P. Lei, X. Liu, Y. Su, L. Dong, J. Feng, H. Zhang, *Nanoscale* **2015**, *7*, 17861.
[224] Y. Huang, A. Skripka, L. Labrador-Paez, F. Sanz-Rodriguez, P. Haro-Gonzalez, D. Jaque, F. Rosei, F. Vetrone, *Nanoscale* **2018**, *10*, 791.
[225] J. Zhou, S. Wen, J. Liao, C. Clarke, S. A. Tawfik, W. Ren, C. Mi, F. Wang, D. Jin, *Nat. Photonics.* **2018**, *12*, 154.
[226] X. J. Zhu, J. C. Li, X. C. Qiu, Y. Liu, W. Feng, F. Y. Li, *Nat. Commun.* **2018**, *9*, 2176.
[227] S. Baral, A. R. Miandashti, H. H. Richardson, *Nanoscale* **2018**, *10*, 941.
[228] A. R. Miandashti, M. Kordesch, H. H. Richardson, *MRS Adv.* **2018**, *3*, 747.
[229] X. S. Cui, Y. Cheng, H. Lin, F. Huang, Q. P. Wu, Y. S. Wang, *Nanoscale* **2017**, *9*, 13794.
[230] D. D. Li, Q. Y. Shao, Y. Dong, J. Q. Jiang, *J. Phys. Chem. C* **2014**, *118*, 22807.
[231] D. D. Li, Q. Y. Shao, Y. Dong, F. Fang, J. Q. Jiang, *Part. Part. Syst. Char.* **2015**, *32*, 728.
[232] Q. Y. Shao, L. L. Ouyang, L. F. Jin, J. Q. Jiang, *Opt. Express* **2015**, *23*, 30057.
[233] Q. Y. Shao, G. T. Zhang, L. L. Ouyang, Y. Q. Hu, Y. Dong, J. Q. Jiang, *Nanoscale* **2017**, *9*, 12132.
[234] L. L. Liang, X. G. Liu, *Nat. Photonics* **2018**, *12*, 124.
[235] E. D. Martínez, J. H. Lohr, M. Sirena, R. D. Sanchez, H. Pastoriza, *Flex. Print. Electron.* **2016**, *1*, 035003.
[236] X. He, A. L. Liu, X. Y. Hu, M. X. Song, F. Duan, Q. M. Lan, J. D. Xiao, J. Y. Liu, M. Zhang, Y. Q. Chen, Q. G. Zeng, *Nanotechnology* **2016**, *27*, 475709.

Figures and Tables

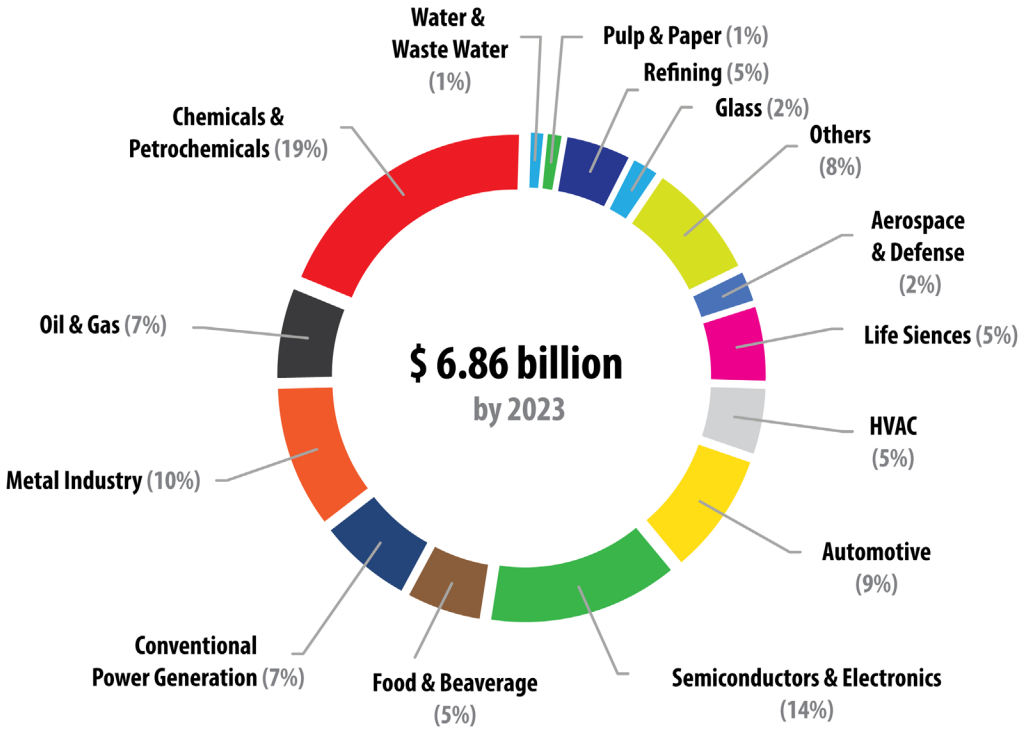

Figure 1. Revenue generation for the global temperature sensors market (Grand View Research Inc.). Adapted from reference [12].

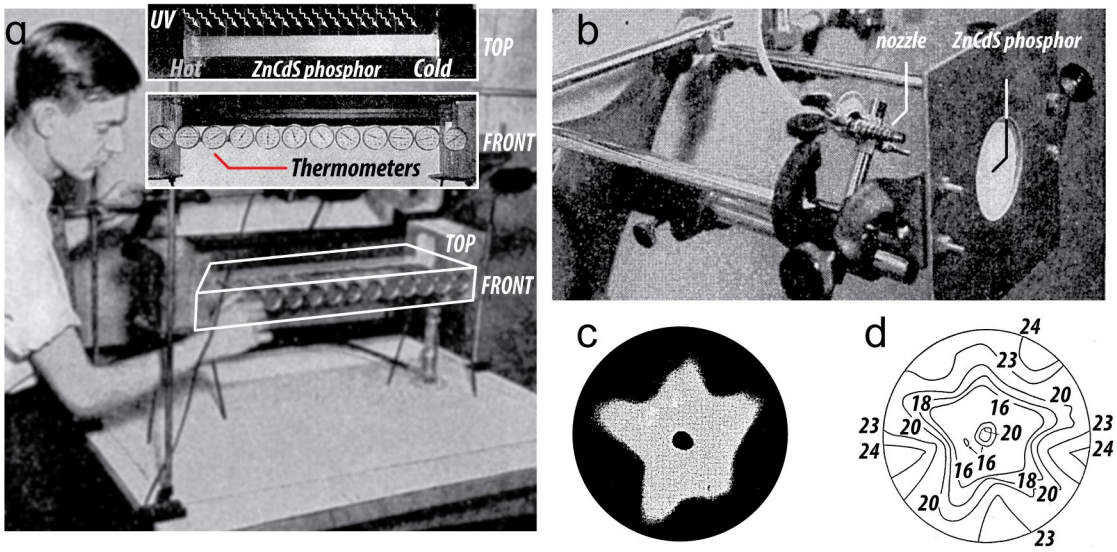

Figure 2. (a) Device for calibrating temperature-sensitive ZnCdS phosphors. The front view of the device displays the thermometers used for calibration, temperature increases from right to the left. The top image shows the phosphor upon UV excitation, with the brighter region corresponding to the lowest temperature. (b) Arrangement for studying air stream impinging upon phosphor screen. (c) High-contrast illustrative print of thermal pattern produced by the air stream. (d) Isotherms on the screen obtained from the set of prints like that presented in (c). Numbers are temperatures in degrees centigrade. Adapted from reference [87]. Copyright (1949), OSA Publishing.

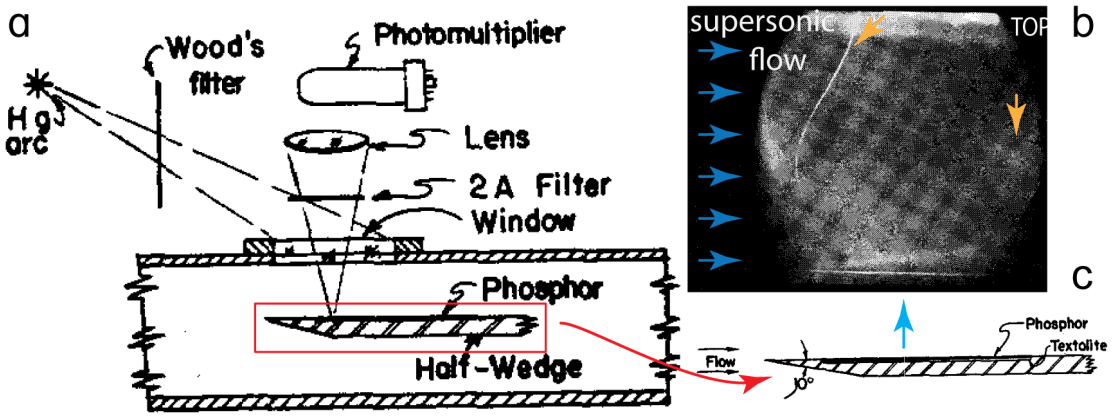

Figure 3. (a) Schematic diagram of optical arrangement for calibration and use of temperature-sensitive ZnCdS phosphors in aeronautics.[88] (b) Photograph of the half-wedge (surface recovered with the phosphor) after 2 s of supersonic flow. The marked bright line is a crack in the phosphor coverage. The brighter parts of the surface are cooler by about 2 degrees than the darker parts and cooler by about 5 degrees than at the beginning of the flow. The bright streaks at the top and bottom of the picture are an indication of the transition between the laminar and turbulent flowing regimes. The marked bright streak at the right center are believed to be due to the beginning of natural turbulence. (c) Detail of the construction of the phosphor coated half-wedge. Adapted from reference [88]. Copyright (1953), AIP Publishing.

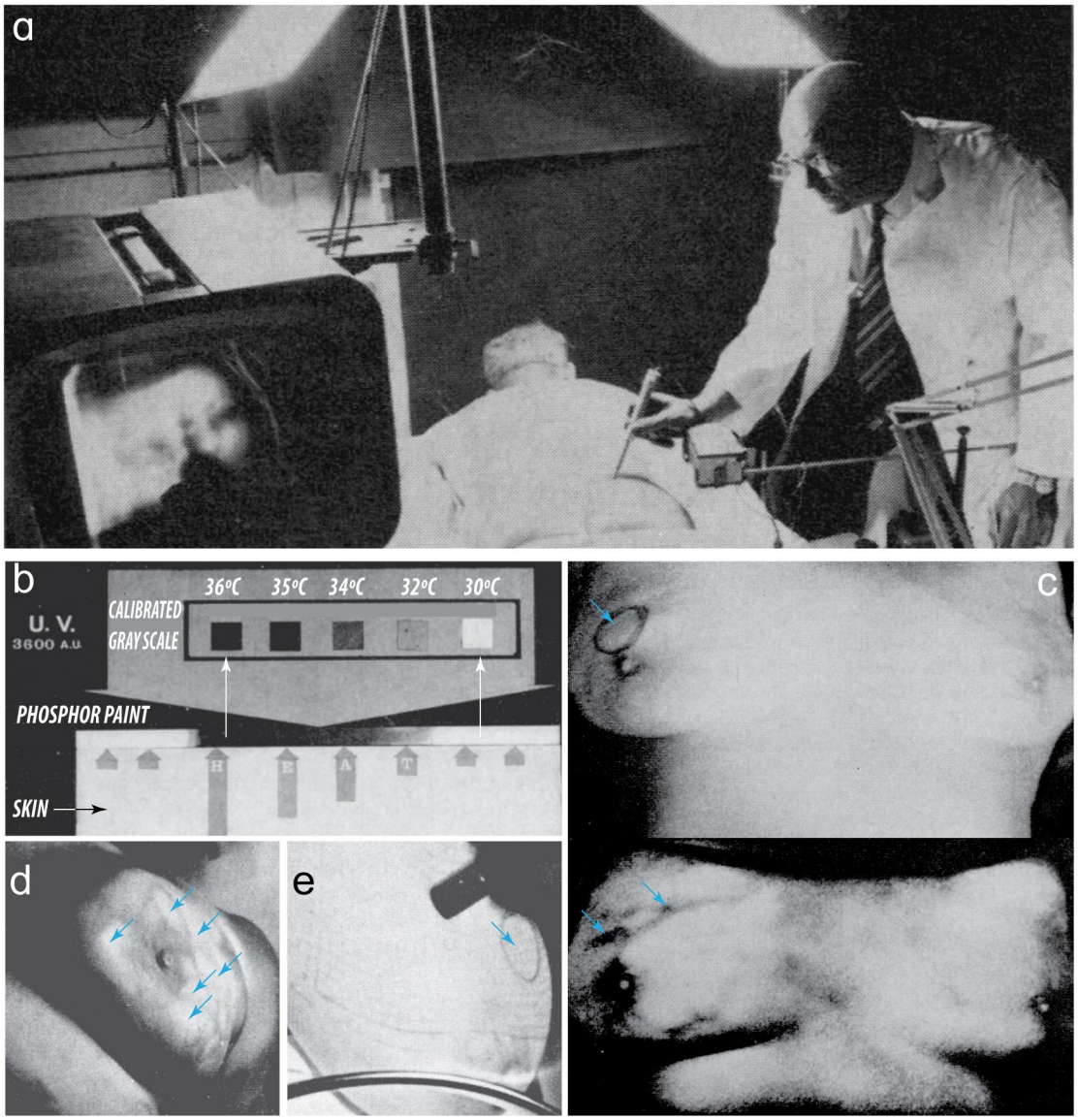

Figure 4. (a) General view of a pioneering thermal imaging setup based on the employment of thermally sensitive phosphors which glow when exposed to ultraviolet illumination, in inverse proportion to the underlying temperature. The thermal image can be directly observed or more critically analyzed and photographed on a simple closed-circuit television monitor. (b) Calibrated gray scale of the heat-quenched of a ZnCdS-based phosphor (in the form of an aerosol spray). Dark areas mean increased temperature. (c) A black-and-white image is converted to a thermogram by switching from room light to ultraviolet. Top view shows an ordinary image of encircled breast lump, whereas bottom is a view under UV irradiation of heat patterns in the skin coated by the ZnCdS-based phosphor. The dark streaks over the tumor (marked with arrows) depict hot veins typical of carcinoma. (d) Breast showing various cold areas (in white, marked with arrows) corresponding to non-malign cysts that can be aspired. The same measurement using a thermistor probe is presented in (e) for comparison, being evident the lower spatial discrimination in comparison with the image in (d). Adapted from reference[90]. Copyright (1965) CMAJ.

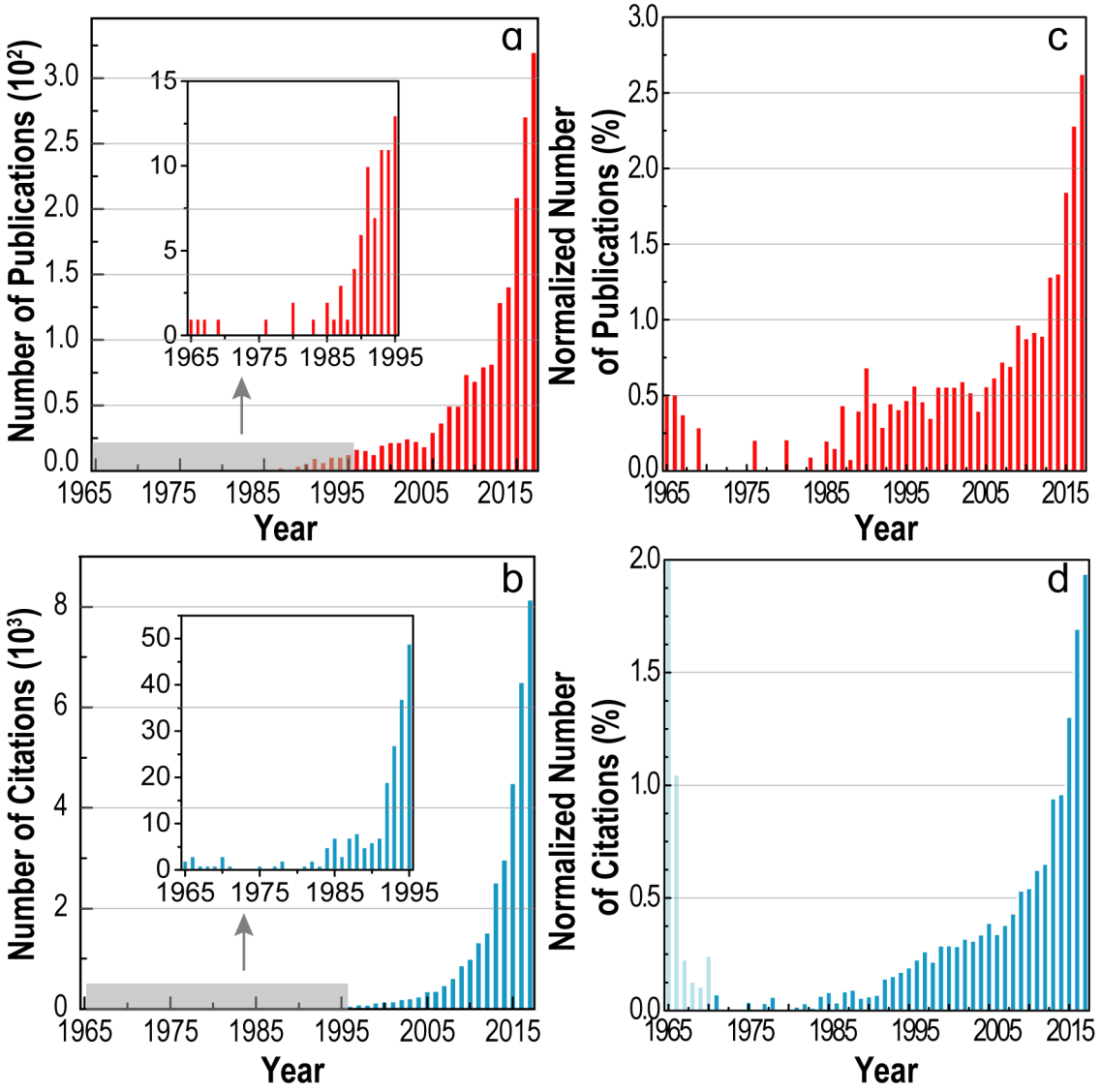

Figure 5. Number of (a) publications and (b) citations of scientific papers using the following search in *Web of Science* (Clarivate Analytics), principal collection (1900–2017): ((luminescence OR fluorescence) AND (thermometry OR nanothermometry)) OR ((luminescent OR fluorescent) AND (thermometer OR nanothermometer)) OR ((upconversion) AND (thermometry OR nanothermometry)) OR (phosphor thermometry) OR (phosphor temperature-measurements) OR (thermographic phosphors), topic, OR (temperature recording with phosphors), title. Panels (c) and (d) display the corresponding normalized data to the keywords (luminescent OR luminescence), topic. The search was performed on 05/06/2018.

https://doi.org/10.1002/adom.201801239

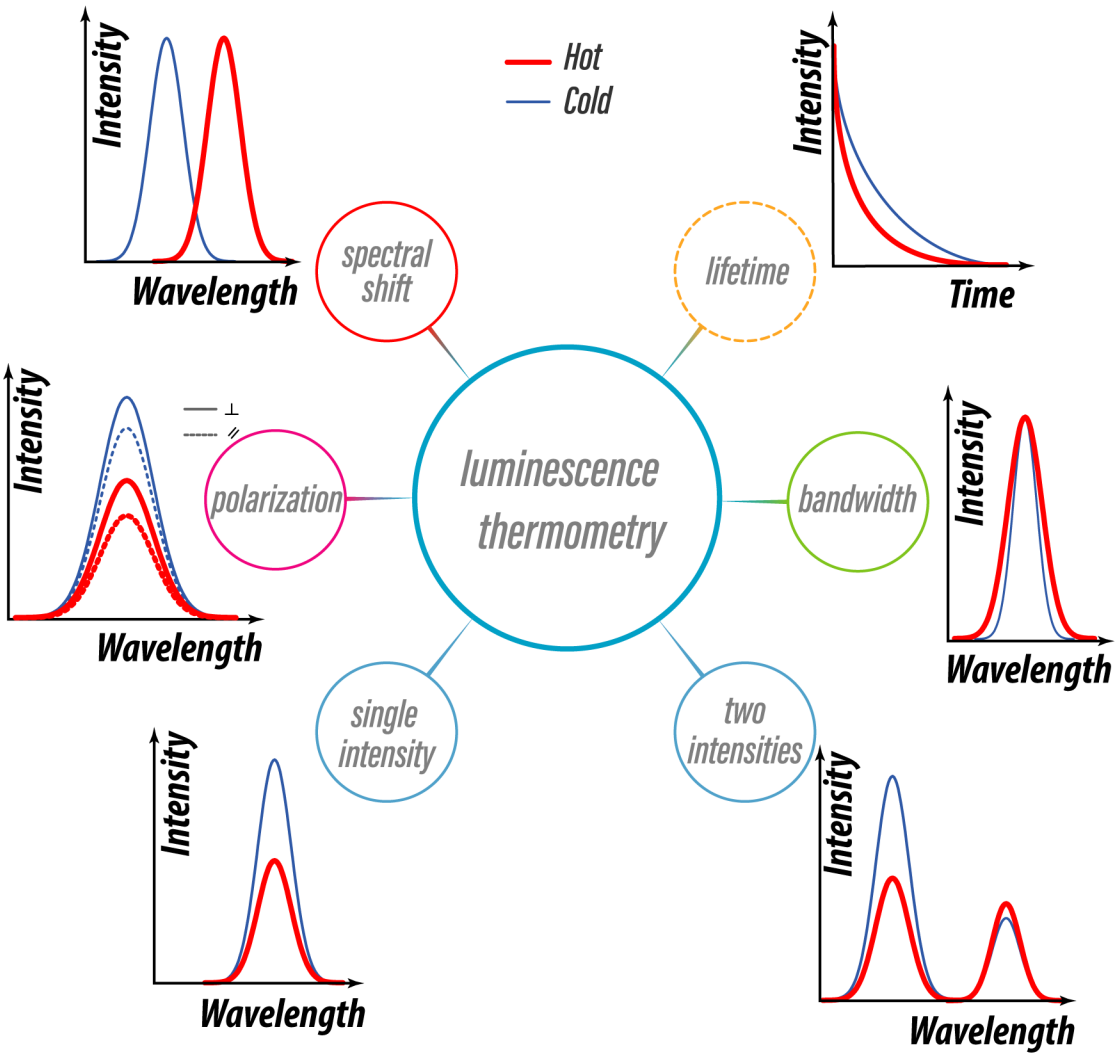

Figure 6. Schematic representation of the possible effects on the phosphors' emission features caused by temperature increasing.

https://doi.org/10.1002/adom.201801239

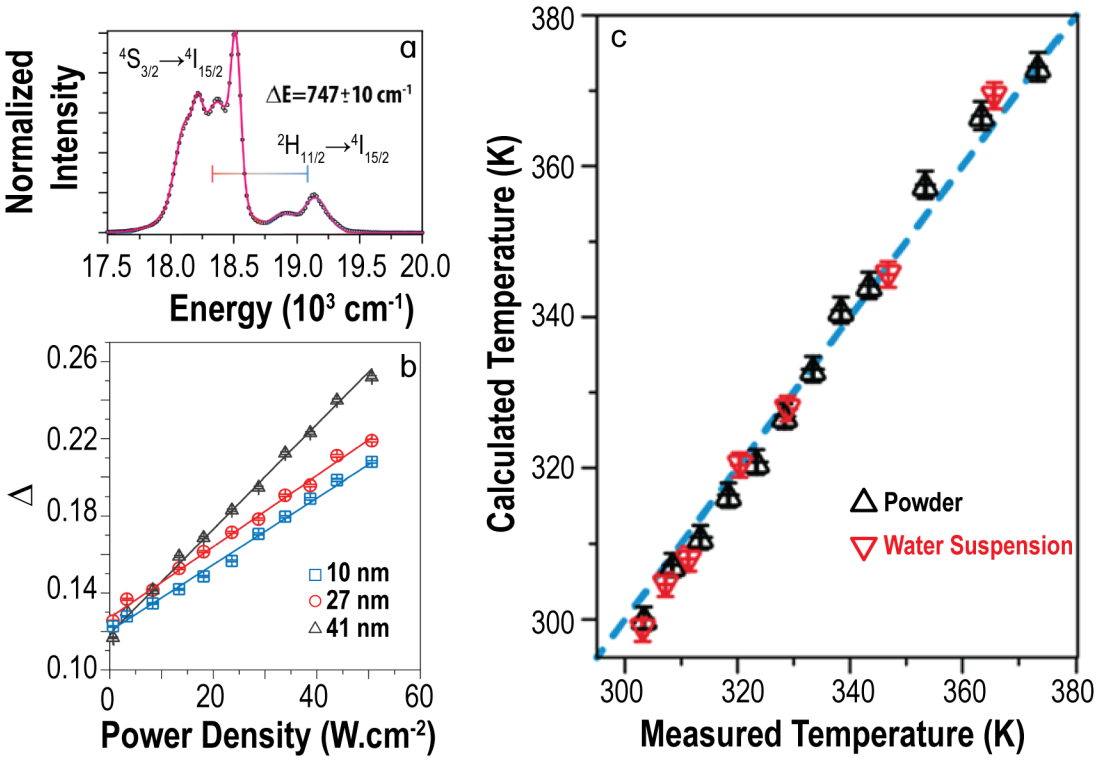

Figure 7. (a) Emission spectrum (points) of $SrF_2:Yb^{3+}/Er^{3+}$ NPs (41 nm) recorded at 300 K using a laser power density of 42±5 W·cm^{-2}. The spectrum was fitted to a set of two and five Gaussian peaks in the $^2H_{11/2}\rightarrow{}^4I_{15/2}$ and $^4S_{3/2}\rightarrow{}^4I_{15/2}$ spectral regions, respectively (not shown). The magenta line assigns the envelope of the sum of the two transitions. (b) Evolution of the thermometric parameter with the laser power density for $SrF_2:Yb^{3+}/Er^{3+}$ NPs of distinct sizes. The value of Δ at no-laser excitation (Δ_0) is determined from the intercept. (c) Calculated temperature using Eq. 12 (y) *versus* temperature reading using a thermocouple (x) of $SrF_2:Yb^{3+}/Er^{3+}$ NPs in powder and water suspension. The dashed line is a guide for the eyes corresponding to $y = x$. The horizontal error bars represent the thermocouple accuracy and the vertical ones the error in the calculated temperature. Copyright (2017), ACS Publishing.[138]

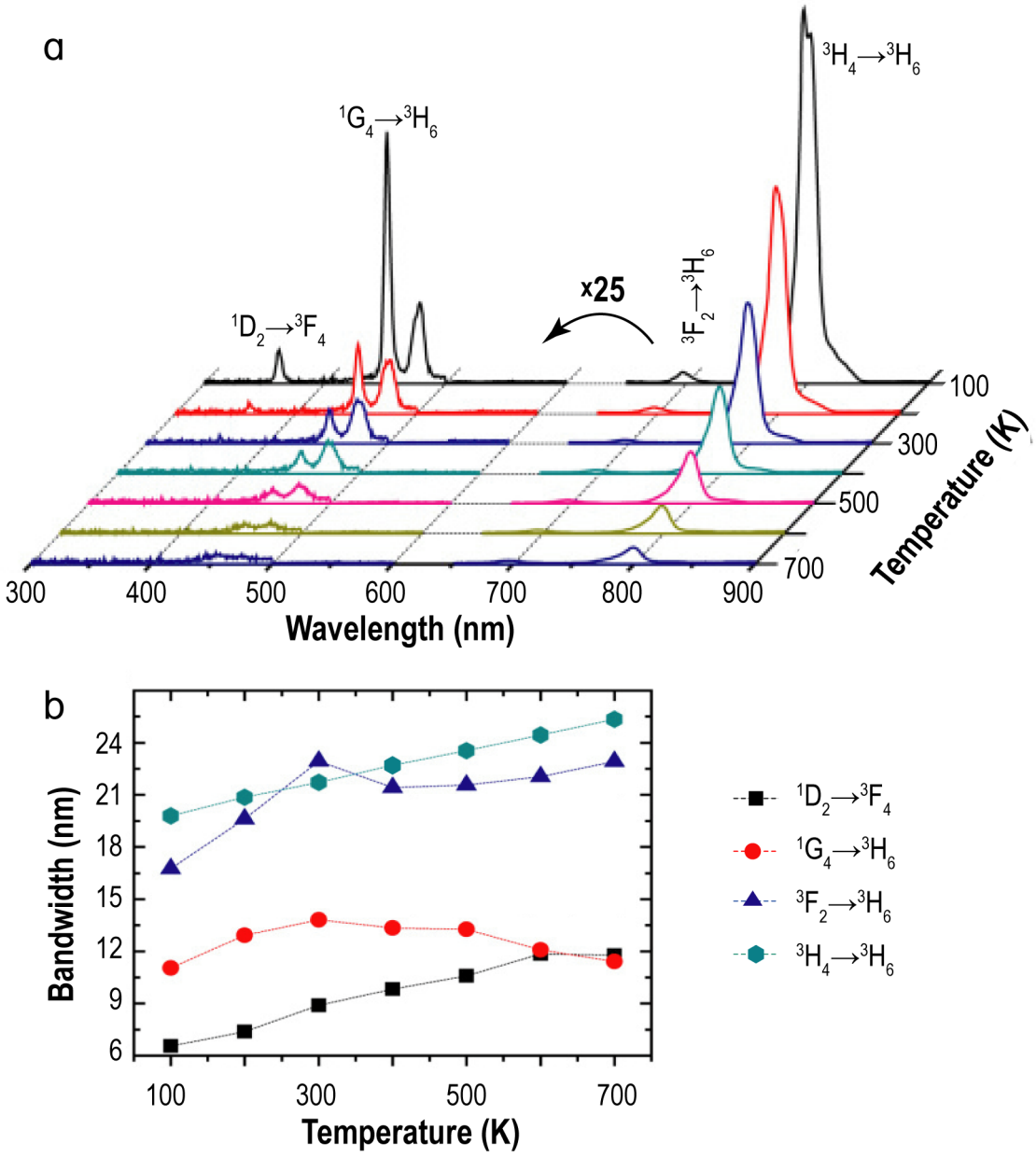

Figure 8. (a) Temperature-dependent Tm^{3+} emissions in $NaYbF_4:Tm^{3+}@SiO_2$ core@shell microparticles. (b) Temperature-dependent bandwidth of distinct Tm^{3+} transitions in $NaYbF_4:Tm^{3+}/SiO_2$. Adapted from reference [162]. Copyright (2013), OSA Publishing.

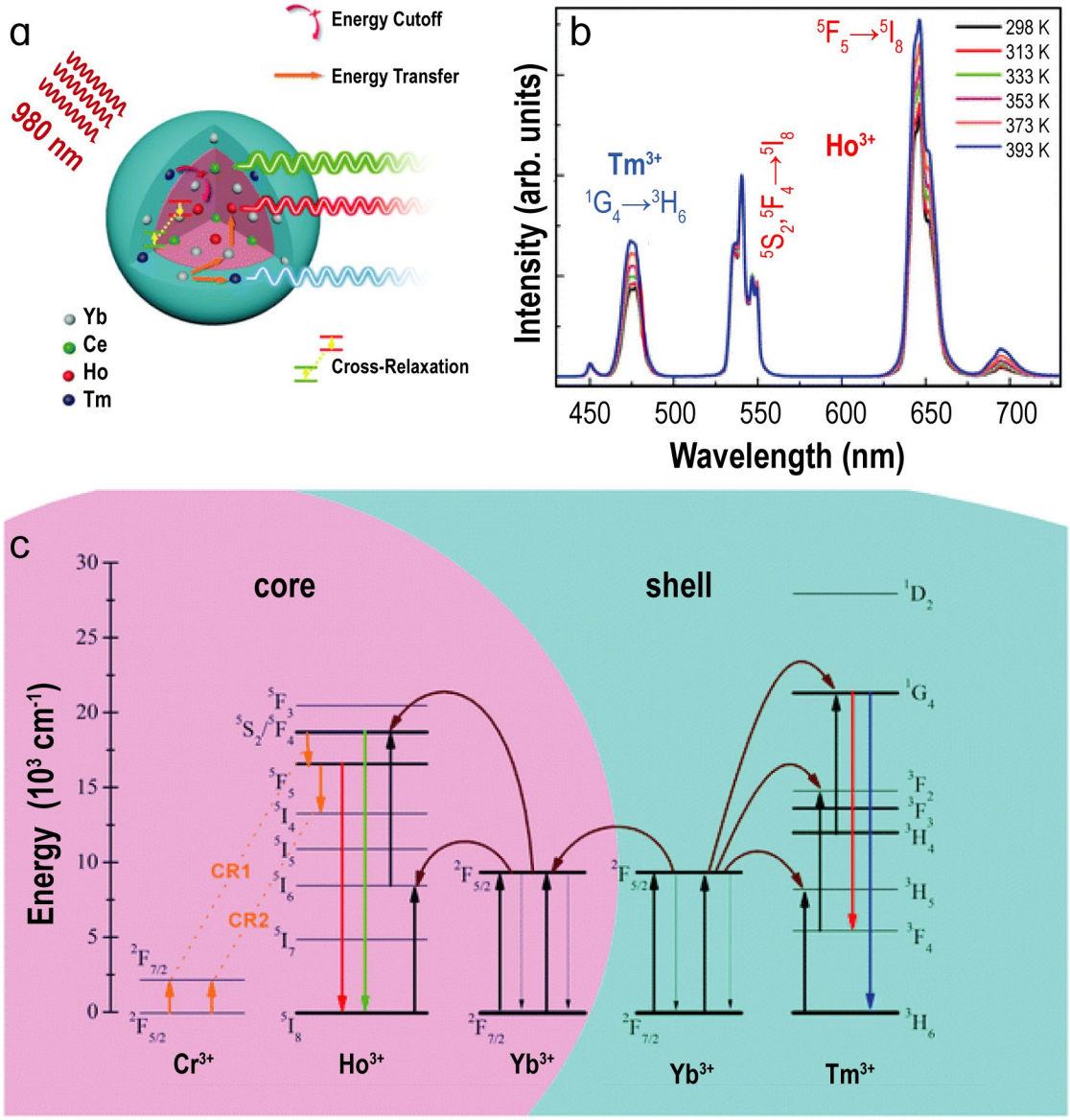

Figure 9. (a) Schematic representation of the Yb/Ho/Ce:$NaGdF_4$@Yb/Tm:$NaYF_4$ core@shell nanostructure. (b) Temperature-dependent UC emission spectra of the nanostructures upon 980 nm excitation, normalized to the emission line at 450 nm. (c) Simplified energy level diagrams of Ce^{3+}, Ho^{3+}, Yb^{3+} and Tm^{3+} with the proposed energy transfer mechanisms. Adapted from reference [206]. Copyright (2016), Royal Society of Chemistry.

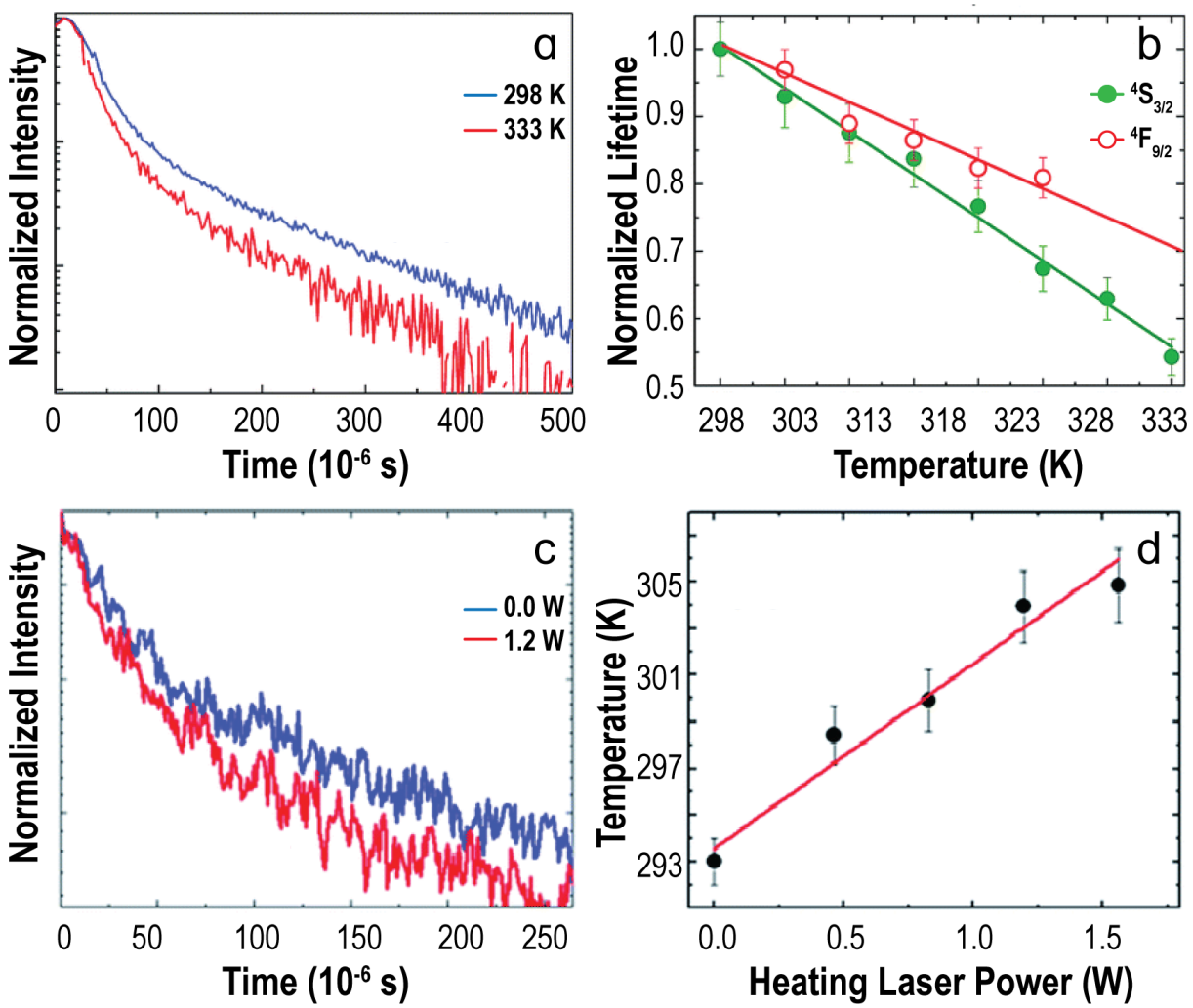

Figure 10. (a) $^4S_{3/2}$ decay curves in $NaY_2F_5O:Yb^{3+}/Er^{3+}$ NPs at 298 and 333 K. (b) Temperature dependence of the normalized $^4S_{3/2}$ and $^4F_{9/2}$ lifetime values. Points represent experimental data and solid lines are the best to the experimental points using straight lines. (c) $^4S_{3/2}$ decay curves measured in NPs injected 1 mm below the surface of a chicken breast when the heating laser was on (1.2 W) or off (0 W). (d) Sub-cutaneous temperature measured using the lifetime values for distinct heating laser power values. Reproduced from reference [58]. Copyright (2014), Royal Society of Chemistry.

https://doi.org/10.1002/adom.201801239

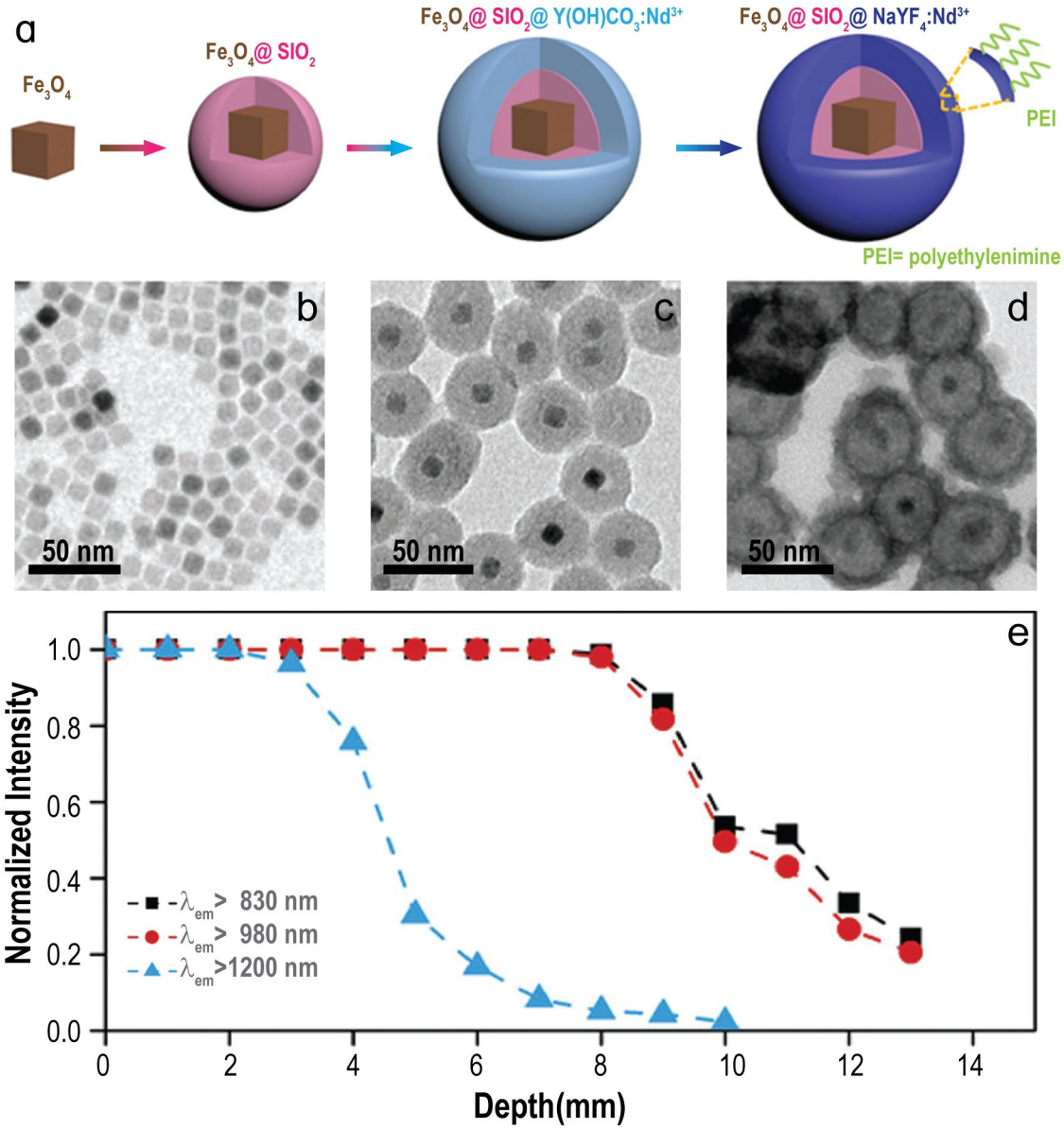

Figure 11 (a) Schematic illustration of the synthetic procedure of Fe_3O_4@SiO_2@$NaYF_4$:Nd^{3+} NPs. TEM images of (b) Fe_3O_4, (c) Fe_3O_4@SiO_2 and (d) Fe_3O_4@SiO_2@ $Y(OH)CO_3$:Nd^{3+} NPs. (e) Normalized intensity of Fe_3O_4@SiO_2@$NaYF_4$:Nd^{3+} NPs as a function of the penetration depth, calculated from imaging *ex-vivo* chicken breast samples (distinct thicknesses) under 806 nm excitation with an optical long-pass filter (830, 980, or 1200 nm) in the emission path. Reproduced from reference[217]. Copyright (2018), John Wiley & Sons.

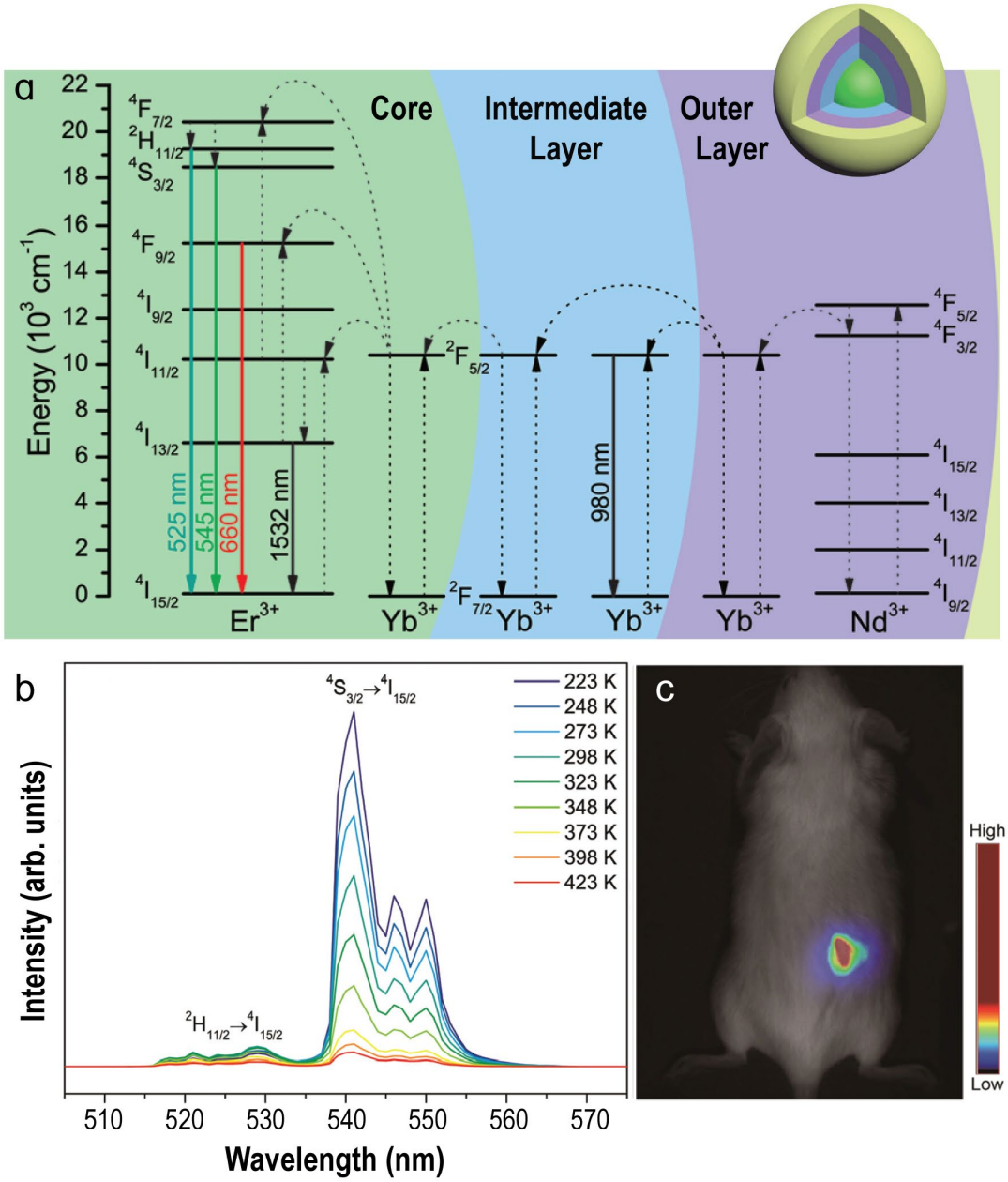

Figure 12. (a) Schematic representation of UC and DS transitions in $NaLuF_4:Gd^{3+}/Yb^{3+}/Er^{3+}@NaLuF_4:Yb^{3+}@NaLuF_4:Nd^{3+}/Yb^{3+}@NaLuF_4$ core@shell nanostructures, depicted schematically in the inset. (b) Emission spectra of the core@shell nanostructures under 808 nm excitation in the 223–423 K range. (c) Overlap between a photograph and a NIR image under 808 nm laser excitation of a mouse subcutaneously injected with aqueous dispersion of the PEG modified core@shell nanostructures. Adapted from reference [223]. Copyright (2015), Royal Society of Chemistry.

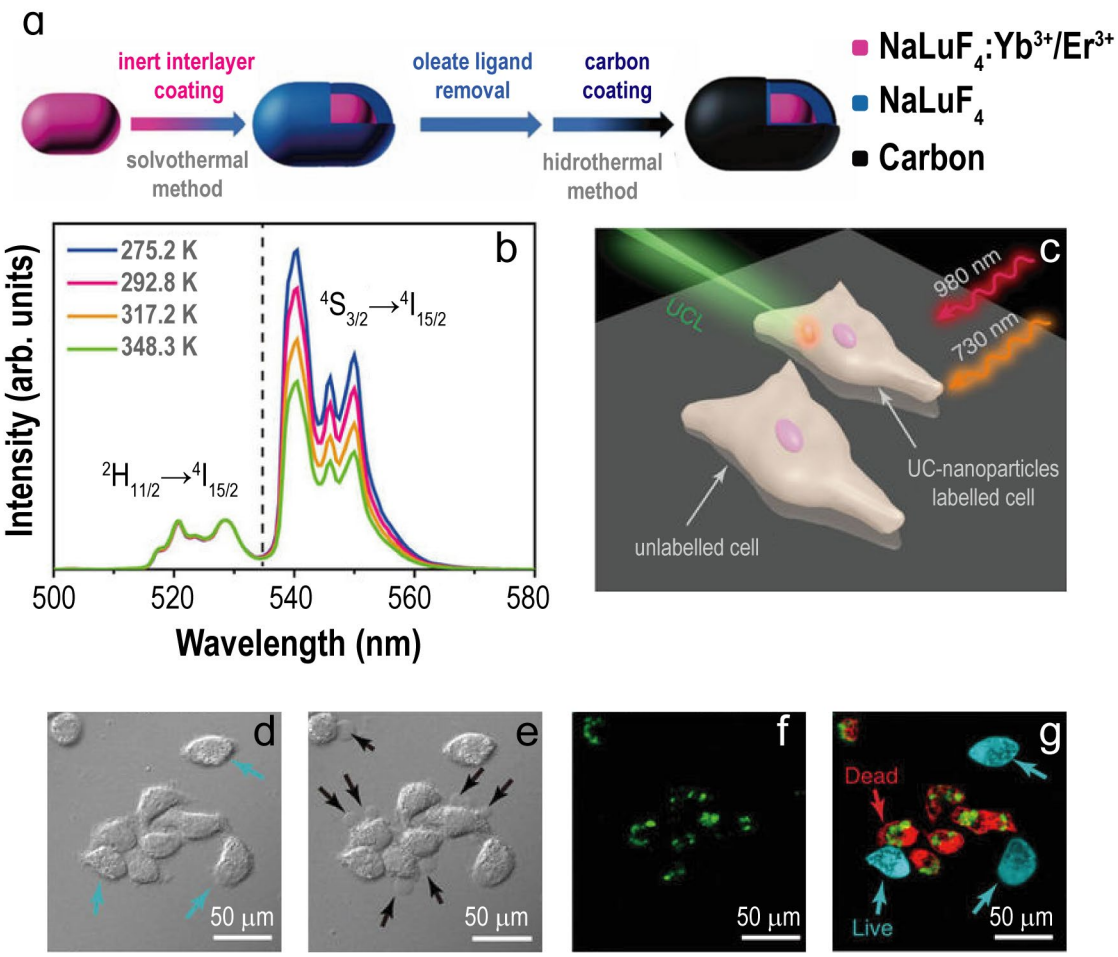

Figure 13. (a) Schematic diagram of the synthetic route of the core@shell UC NPs. (b) UC emission spectra of core@shell NPs at different temperatures. (c) Schematic diagram of photothermal therapy in cells. Microscopy images of HeLa cells treated with photothermal ablation or external heating. Bright field image of unlabeled cells (d) before and (e) after irradiation with a 730 nm laser (0.3 W cm^{-2}). Microscopy image of (f) UC emission (under 980 nm excitation). (g) Superimposition of UC and double-stained cells images after irradiation by 730 nm laser (0.3 W cm^{-2}) using calcein-AM (acetoxymethyl) and propidium iodide to stain life and dead cells, respectively. Adapted from reference [57]. Copyright (2016), Springer Nature.

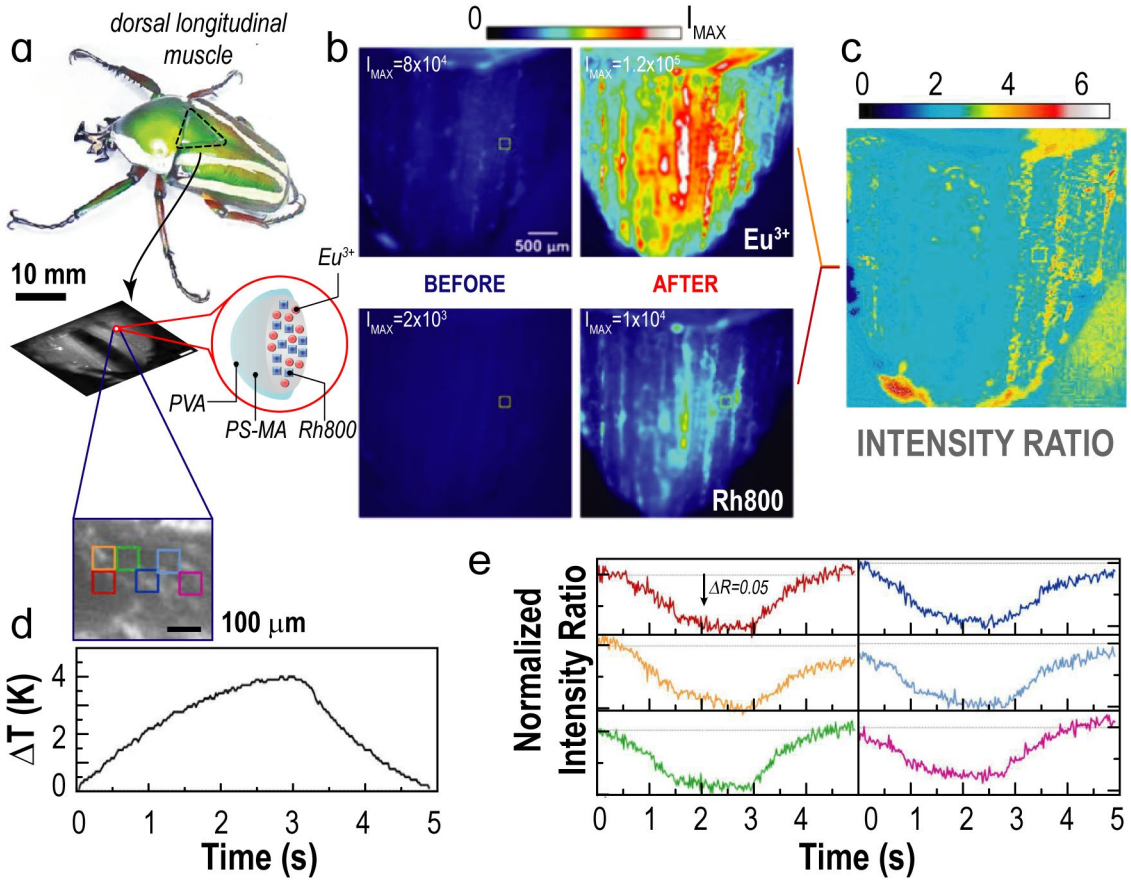

Figure 14. (a) Photograph of a *Dicronorrhina derbyana* beetle with a detail of the dorsal longitudinal muscle (a major flight muscle of the beetle) in which the ratiometric thermosensor was loaded (dashed triangle). Inset shows a photo of the muscle and a schematic representation of the nanoparticle. (b) Pseudocolor images of the intensity of the Eu^{3+} and Rh800 channels before and after the deposition of the thermometer. (c) Intensity ratio of the Eu^{3+} and Rh800 channels that is function of the temperature. (d) Temporal thermal profile performed by an IR thermometer of the region presented in the inset of (a). (e) Corresponding temporal profiles of the normalized intensity ratio in the distinct regions marked in the inset of (d). Adapted from reference [121, 122]. Copyright (2016), American Chemical Society.

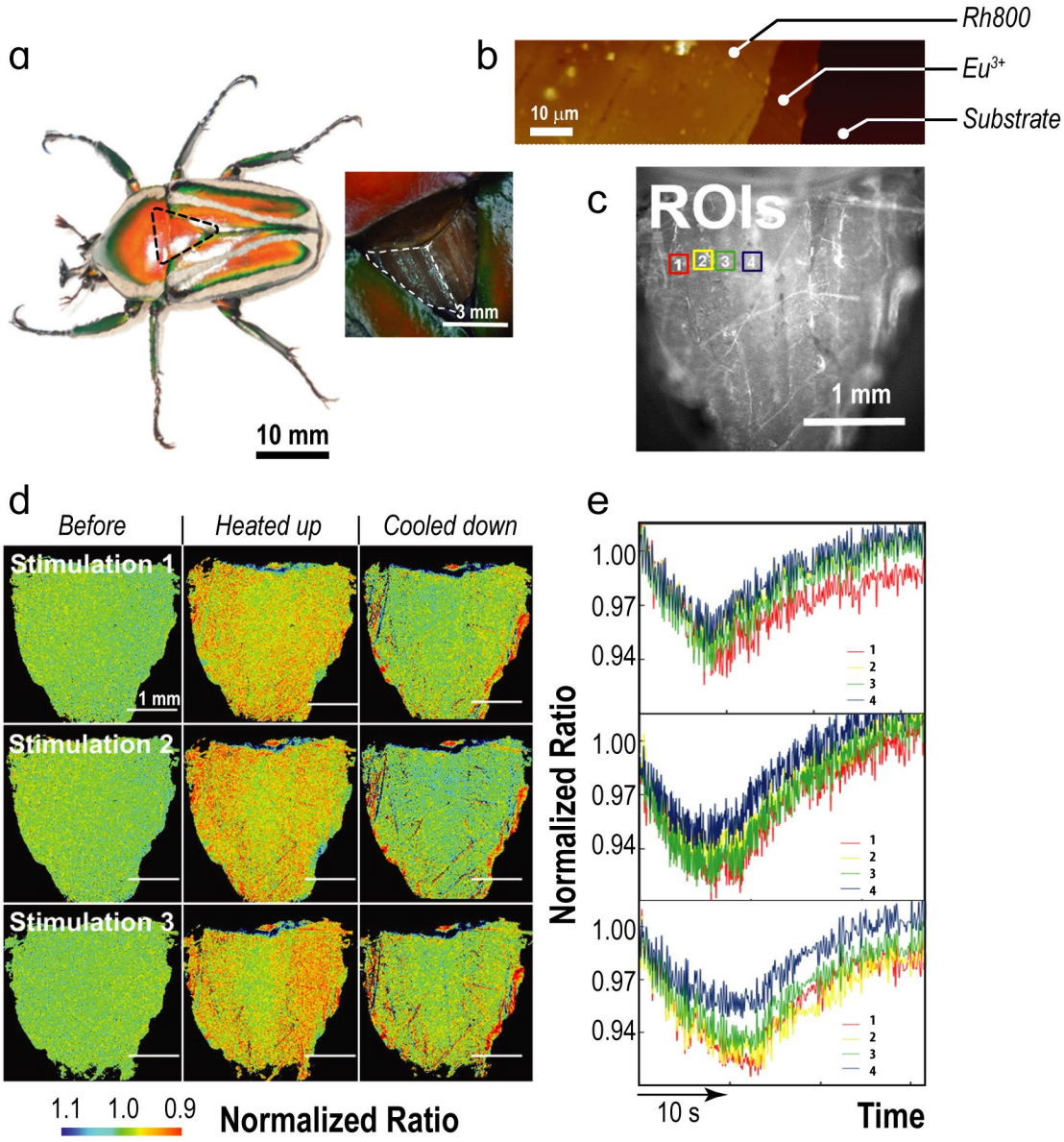

Figure 15. (a) Bright-field image of a *Dicronorrhina derbyana* beetle. The triangle (magnified in the insert) marks the location of the stacked nanosheets attached to the dorsal longitudinal muscle. (b) AFM image of the stacked nanosheets deposited onto a SiO_2 substrate. (c) Photograph of the dorsal longitudinal muscle presenting the location of the regions of interest (ROI) further mapped by the luminescent thermometer. (d) Temperature mapping (three stimulations) of the muscle before (left), during (middle), and after (right) beetle's pre-flight preparation using the stacked nanosheets. (e) The corresponding temporal evolution of the normalized Eu^{3+}/Rh800 intensity ratio in the three stimulations, followed in the ROI areas presented in (c). Adapted from reference [121, 122]. Copyright (2016), American Chemical Society.

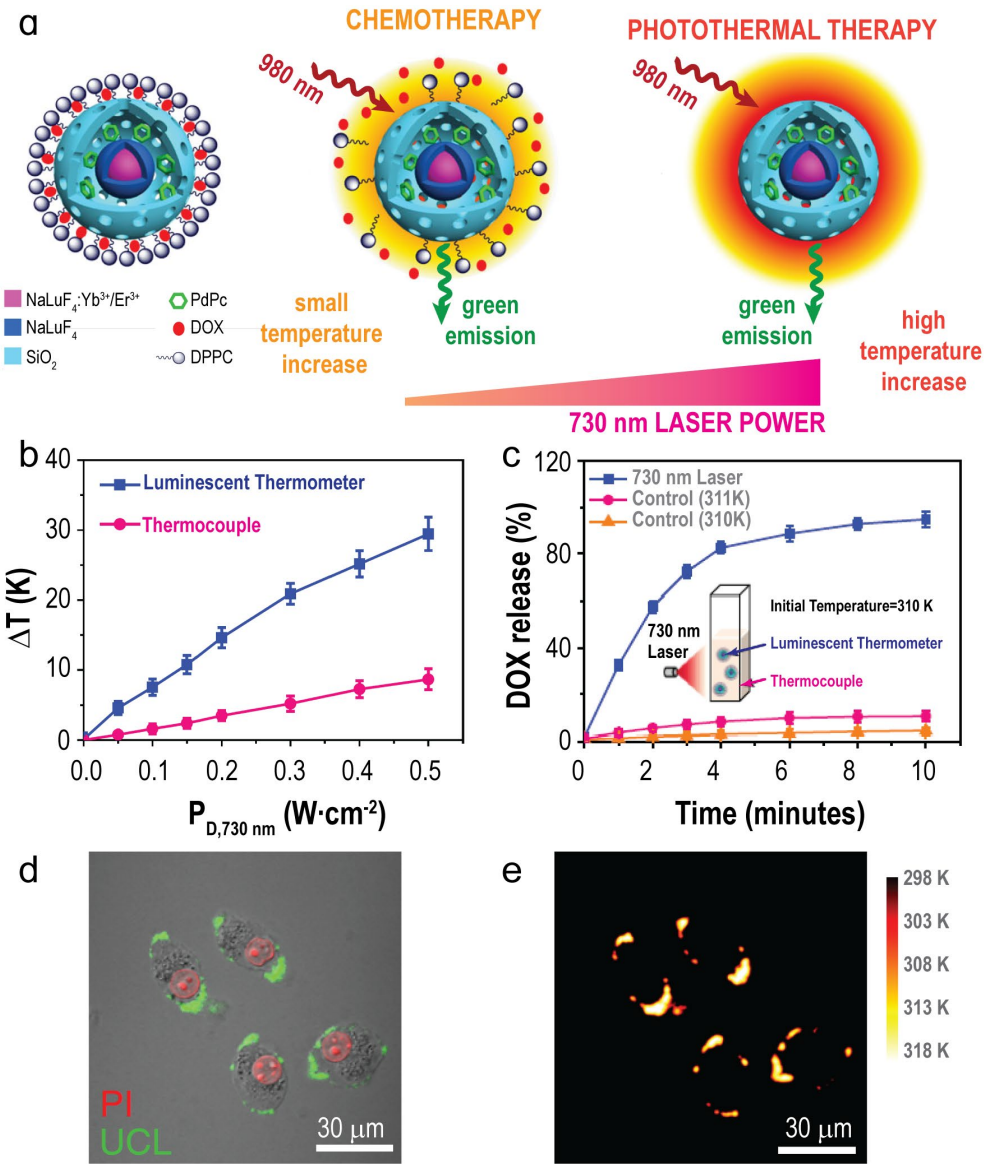

Figure 16. (a) Temperature responsive $NaLuF_4:Yb^{3+}/Er@NaLuF_4@Yolk\text{-}Shell\text{-}SiO_2$-PdPc@DPPC-DOX nanosystem. The temperature is monitored by the UC emission (980 nm excitation). The power density of the photothermal excitation source (730 nm) can be tuned accurately to initiate a thermal-controlled drug release and PTT stepwise. (b) Temperature increase of an aqueous suspension of the NPs (0.5 g L^{-1}) at various power densities. (c) DOX release rate with time for an aqueous suspension of the NPs (50 W cm^{-2}). Control experiments at distinct temperatures are also presented. (d) Emission of the UCNPs and propidium iodide (denoted by UCL and PI, respectively) and (e) temperature imaging during PTT with 730 nm laser irradiation (0.140 W cm^{-2}). The temperature imaging was performed using the Er^{3+} UC emission in the green spectral region. The cells were dead as their nucleuses could be stained with propidium iodide. Adapted from reference [226]. Copyright (2018), Springer Nature.

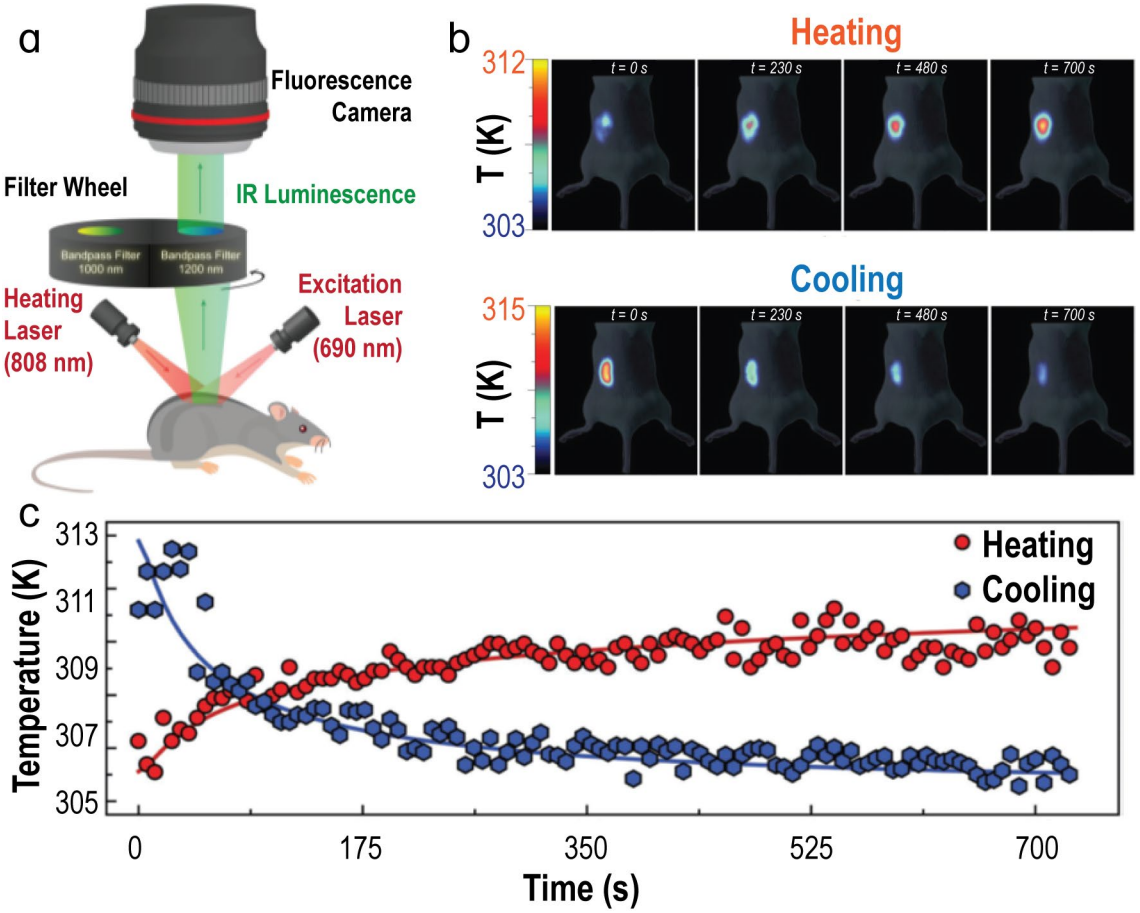

Figure 17. (a) Scheme of the in vivo 2D subcutaneous dynamic thermal imaging experiment. Thermal images obtained by dividing the luminescence images at 1000 and 1200 nm during (b) heating and (c) cooling processes. An optical figure of the anesthetized mouse was superimposed. (d) Time evolution of the average temperature of the injection area as measured by the luminescent thermometers during heating and thermal relaxation processes. Adapted from reference [123]. Copyright (2017), John Wiley & Sons.

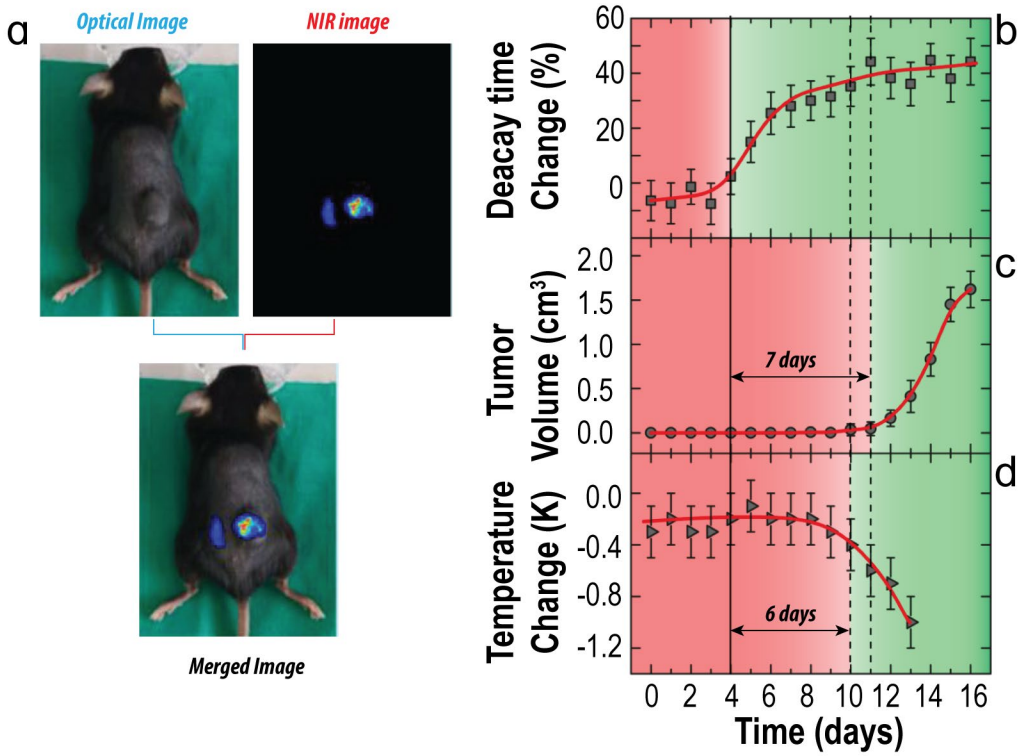

Figure 18. (a) Optical and NIR fluorescence images of a representative mouse. The NIR emission evidences the presence of Ag_2S nanocrystals both at the tumor site and in a healthy tissue area. (b) Time evolution after tumor induction (day zero) of $\Delta\tau$ (normalized difference between the thermal relaxation time of tumoral tissue with respect to that of the healthy tissue). (c) Time evolution of tumoral volume. (d) Time evolution after tumor induction of the surface temperature difference between tumor and healthy tissue as obtained with a thermographic camera. In all cases, the dots correspond to the experimental data obtained as an average of the n = 6 mice analyzed in this work and solid lines are included as guides for the eyes. The background colors and vertical lines indicate the time when the tumor becomes detectable by the different methods.

https://doi.org/10.1002/adom.201801239

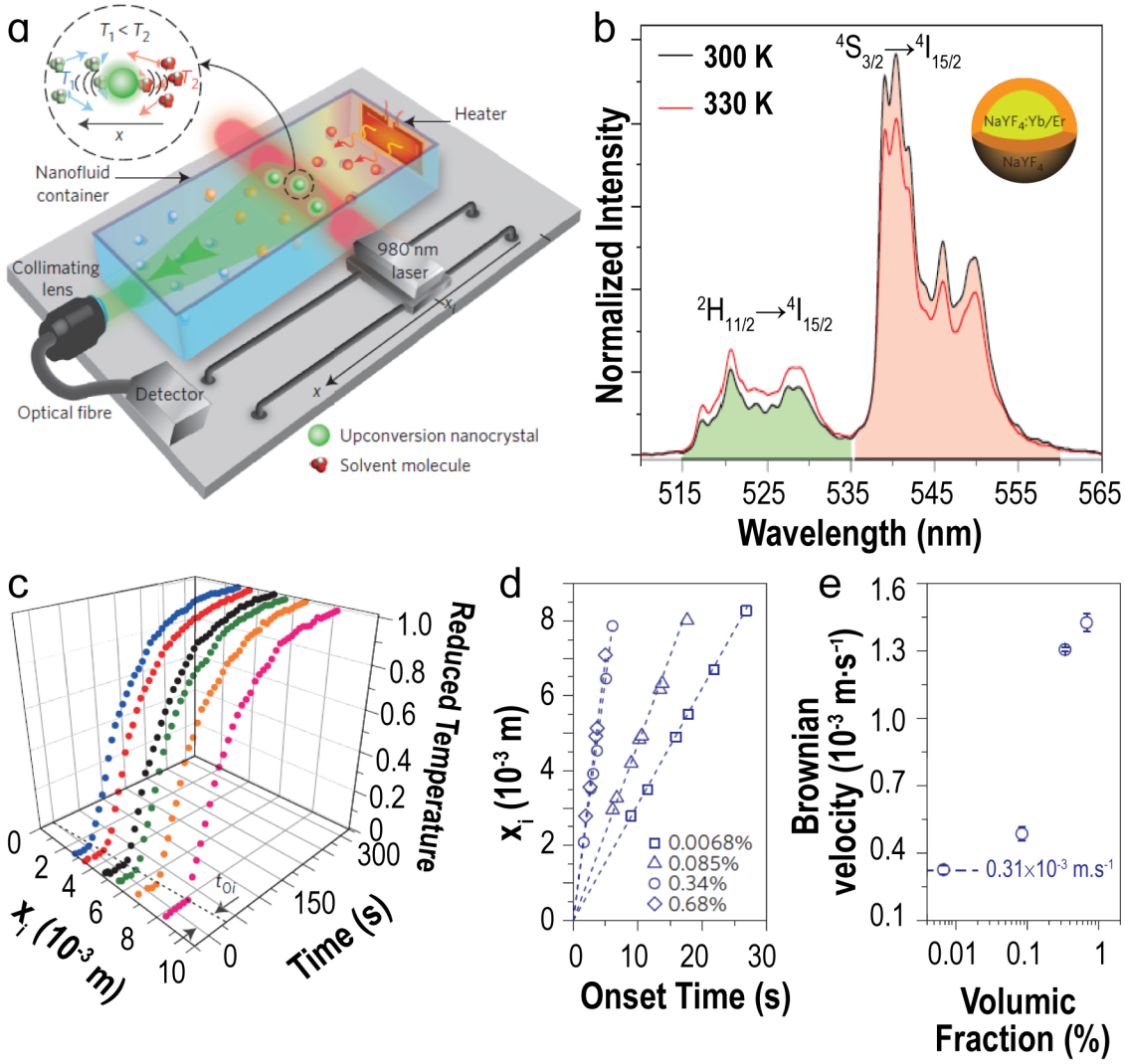

Figure 19. (a) Schematic of the experimental set-up used to determine the instantaneous Brownian velocity of the $NaYF_4:Yb^{3+}/Er^{3+}$@$NaYF_4$ nanofluid. The inset shows the solvent-mixing effect arising from the Brownian motion of the nanoparticle located at the interface between the cold (T_1) and hot (T_2) regions of the nanofluid. (b) Emission spectra of the water-based nanofluid (ϕ=0.0068%) recorded at 300 and 330 K. The spectra were normalized to the maximum intensity of the $^4S_{3/2} \rightarrow {}^4I_{15/2}$ emission at 300 K. The inset presents a scheme of the core@shell NP. (c) Reduced temperature profiles of the NPs dispersed in water (0.0068%) as measured by laser excitation from different positions x_i along the x direction (depicted in (a)). The dashed line refers to the critical onset time t_{0i} when the onset of change in the intensity ratio is observed due to temperature variation upon turning on the heater. (d) The corresponding linear correlation (r^2> 0.994) between x_i and t_{0i}, as measured in water for the nanofluids with different nanoparticle volume fractions. (e) Measured Brownian velocities of the NPs in water as deduced from (c). The horizontal line marks the velocity in the limit of low dilution. Adapted from reference [128]. Copyright (2016), Springer Nature.

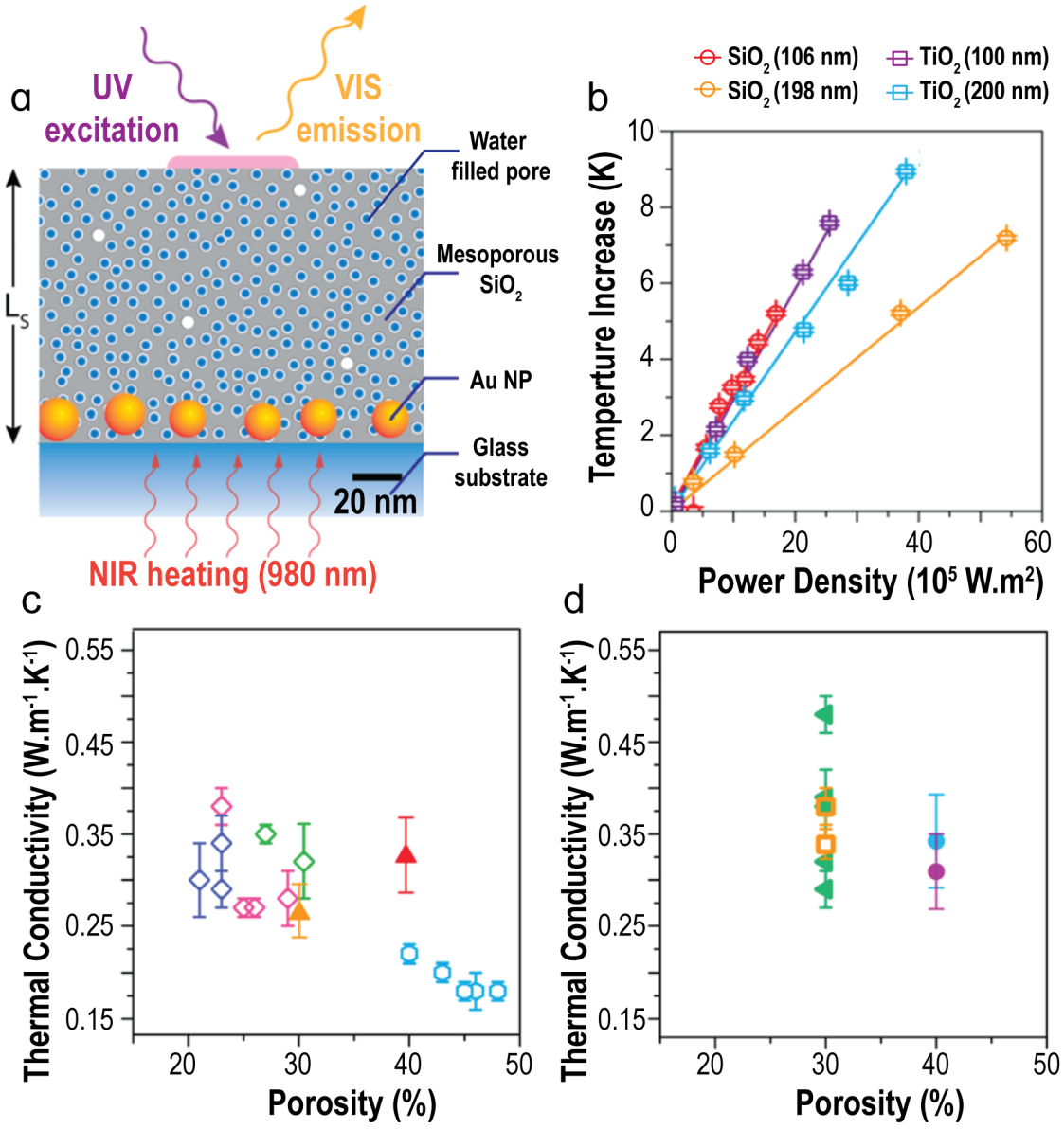

Figure 20. (a) Scaled model of the mesoporous nanostructures with the Au NPs. (b) Linear dependence of the temperature increment with the 980-nm laser power density. Comparison between the thermal conductivity values calculated using luminescence thermometry (filled symbols) and the thermal conductivity values reported in the literature computed by conventional electrical methods. Reproduced from reference [129]. Copyright (2017), American Chemical Society.

Biographies &Table of Contents

Dr. Carlos D.S. Brites is a researcher in CICECO- Aveiro Institute of Materials of University of Aveiro. He obtained his Ph.D. in 2012 from the Department of Physics, University of Aveiro, and was a post-doc in the same department. His current research interests include the use of trivalent lanthanide ions as nanoscale luminescent probes for quantifying material's properties.

Dr. Sangeetha Balabhadra is a Postdoctoral fellow in the School of Physical and Chemical Sciences, in University of Canterbury (New Zealand). She obtained her Ph.D. in Physics in 2017 from Department of Physics and CICECO-Aveiro Institute of Materials (Portugal). Her current research interests include synthesis and spectroscopy studies of lanthanide doped nanoparticles.

Prof. Luís D. Carlos is Full Professor in the Department of Physics at the University of Aveiro and vice-director of the CICECO-Aveiro Institute of Materials (Portugal). He is member of the Lisbon Academy of Sciences and of the Brazilian Academy of Sciences. His current research interests include luminescent nanothermometers, luminescent solar concentrators, organic-inorganic hybrids for green photonics (solid-state lighting and integrated optics), and single-ion and single-molecule magnets.

https://doi.org/10.1002/adom.201801239

The field of luminescent thermometers based on lanthanide-bearing materials is reviewed, from the first developments of the field in the 1950-1960's until the most recent cutting-edge examples. The main concepts, ideas and grand challenges are discussed, including the current movement towards the use of luminescent thermometry as a tool in bioimaging and for nanoscale probing.

Keywords: luminescence thermometry, temperature, thermal imaging, lanthanide ions, nanothermometers

Carlos D. S. Brites, Sangeetha Balabhadra and Luís D. Carlos*

Lanthanide-based thermometers: At the cutting-edge of luminescence thermometry

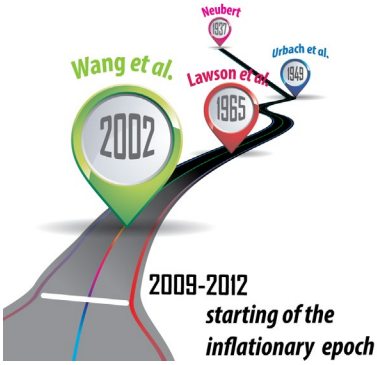

https://doi.org/10.1002/adom.201801239